Analysis of wall mass transfer in a turbulent pipe flow combining extended POD and FIK identity

Rasmus Korslund Schlander and George Papadakis*

Department of Aeronautics, Imperial College London,

London SW7 2AZ, United Kingdom

Stelios Rigopoulos

Department of Mechanical Engineering,

Imperial College London, London SW7 2AZ, United Kingdom

(Dated: February 9, 2022)

Abstract

We combine extended proper orthogonal decomposition (EPOD) together with the Fukagata-Iwamoto-Kasagi (FIK) identity to quantify the role of individual coherent structures on the wall mass transfer in a turbulent pipe flow. Direct numerical simulation (DNS) at a Reynolds number of 5300 (based on bulk velocity) is performed with the passive scalar released at the pipe inlet. The proper orthogonal decomposition (POD) eigenvalues show that the scalar field can be described by a more compact set of modes compared to the velocity field, and that these modes are skewed towards higher azimuthal wavenumbers. POD modes for the scalar and EPOD modes for the velocity are visualized in the cross-stream plane to infer the capacity of each mode to transport scalar to and from the wall. A form of the FIK identity is derived for the wall mass transfer coefficient (Sherwood number, Sh) and employed to separate the contributions of the mean and fluctuating velocity and scalar fields. The FIK decomposition shows that the turbulent velocity/scalar correlations account for up to 65.8% of the total Sh. The contribution of each POD and EPOD mode to the Sh number is also computed; it is found that, using azimuthal wavenumbers $m = 1 - 15$ and POD modes $n = 1 - 10$, it is possible to reconstruct 49% of the turbulent component of Sh, with the velocity modes containing only 31% of the turbulent kinetic energy. Quadrant analysis shows that these modes are related to ejection and sweep events near the wall, with the ejection events dominating.

* Corresponding author: g.papadakis@imperial.ac.uk

I. INTRODUCTION

Organized flow motions, or coherent structures, play an important role in momentum and scalar transport in wall-bounded turbulent flows. These structures have different streamwise and spanwise length scales and several types have been identified, for example near-wall streaks, hairpin or horseshoe vortices, as well as large or very large scale motions (LSM or VLSM), [1–4]. Understanding the relationship between these structures and scalar transport can lead to better control and optimisation of heat and mass transfer to the walls of pipes and channels. For this reason, many studies have investigated the role of coherent structures on scalar transport, both experimentally and computationally; Refs. [5–12] constitute a small sample from an extensive literature. These structures have also been analysed using different types of modal decomposition techniques. For example, in Dawson *et al.* [13] and Laskari *et al.* [14], resolvent analysis was used to analyse DNS, planar PIV and aero-optic scalar and velocity measurements. In Mallor *et al.* [15], modal decomposition was employed to analyse flow fields and heat transfer for wall-proximity square ribs, in order to educe coherent structures and analyse their effect on the instantaneous wall heat flux.

In the present paper, we consider the turbulent flow inside a circular pipe and examine the contribution of individual structures on the time-average mass transfer coefficient (Sh number). We extract the structures using proper orthogonal decomposition (POD), a technique that decomposes the velocity field into a set of orthonormal modes, ranked in terms of their turbulent kinetic energy [16, 17]. Pipe flows have previously been analysed with POD using data from both experiments and numerical simulations. Duggleby *et al.* [18] performed one of the first analyses using DNS data at $Re_\tau = 150$. Baltzer *et. al.* [19] considered higher $Re_\tau = 685$ and found that LSM-like structures were aligned in a helical pattern and suggested that these structures caused the formation of VLSM. A similar result was also found in Hellstrom *et al.* [20], who used a dual-plane PIV setup to probe the flow at a Reynolds number of $1.04 \cdot 10^5$. Lee *et al.* [21] analysed the spatial organization patterns of LSMs and VLSMs, as well as their statistical properties. Abreu *et al.* [22] studied the near-wall streaks in a turbulent pipe flow at $Re_\tau = 180$ and 550 using spectral POD (an extension of POD to the frequency domain) and resolvent analysis, and focused on comparing the two methods.

All the aforementioned pipe flow studies have focused on the velocity field only. In the

present work, our objective is to analyse the effect of the velocity field on a passive scalar. Flow structures obtained from standard POD analysis are ranked with respect to their kinetic energy, and are not necessarily the most effective in terms of scalar transport. The extended proper orthogonal decomposition (EPOD) method, proposed in Ref. [23], is a generalisation of the standard POD and more suitable for our purposes. This technique uses the temporal basis from the decomposition of one variable (in our case, the scalar) in order to decompose another synchronized variable (the velocity). EPOD has been used previously to analyse correlated events, such as velocity in two different regions [24], pressure and velocity fluctuations [25], temperature and velocity fluctuations in wall heated pipes [26], passive scalars in swirling jets [27], and flame dynamics [28]. A related method, known as cross proper orthogonal decomposition (CPOD), was recently proposed [29]. This method decomposes a flow in terms of modes that are ranked according to the cross-correlation they carry, for example Reynolds shear stresses or velocity-scalar correlation. In the present paper, we use EPOD velocity modes that share the same temporal coefficients with the scalar POD modes.

POD and EPOD analyse only the fluctuating components of the velocity and scalar fields. For example, Mallor *et al.* [15] used POD to identify the fluctuating patterns of heat flux on the plate. From the engineering perspective however, we are interested in the time-average wall heat or mass transfer coefficients. To relate the fluctuating components (and thus flow structures) to the time-average coefficient, an equation similar to the Fukagata-Iwamoto-Kasagi (FIK) identity [30] is applied for the scalar. This identity was first derived as a tool for investigating the contribution of Reynolds stress to the skin friction coefficient in channel, pipe and flat boundary layer flows. Similar equations have since been derived to analyse contributions to the Nusselt number in boundary layer and pipe flows [31–36]. In this paper, the identity is applied for the Sherwood number Sh, the non-dimensional gradient of concentration at the wall (equivalent to Nusselt number for mass transfer), and employed to quantify the contribution of individual POD and EPOD modes to the time-average wall mass transfer rate. Thus the coherent structures that have the biggest contribution to Sh can be identified.

To the best of our knowledge, such an investigation has not been reported in the literature before for scalar, but it is the type of analysis that can offer significant benefits. For example, the understanding of the effect of different structures on the near-wall behaviour and in

particular the skin friction coefficient (the equivalent of Sh for momentum transfer) has recently led to the design of actuation schemes for drag-reduction that offer net-power savings even at high Reynolds numbers, see [37]. In the present paper, we apply the idea to a relatively low Reynolds number, but the same approach can be applied to higher Reynolds and Schmidt numbers (to study for example the effect of large scale structures that reside on the log layer on heat/mass transfer coefficient). It is envisaged that the present analysis can motivate schemes that optimise the transfer coefficient (either minimise or maximise, depending on the application), in the same way this has been done for the skin friction coefficient.

The article is structured as follows: the case examined, computational details, and validation of the DNS dataset are presented in section II. The following section III summarizes the POD and EPOD methods. The description of the FIK identity and its application to the dataset is detailed in section IV. The POD and EPOD eigenvalues, mode shapes, and the individual contributions to wall transfer rate are presented and discussed in section V. We conclude in section VI.

II. CASE EXAMINED, COMPUTATIONAL METHOD AND VALIDATION

We consider the turbulent flow inside a circular pipe with a passive scalar injected at the inlet. The flow is assumed to be incompressible and the continuity, momentum and scalar transport equations are written in Cartesian tensor notation as:

$$\frac{\partial u_i}{\partial x_i} = 0, \tag{1}$$

$$\frac{\partial u_i}{\partial t} + \frac{\partial u_i u_j}{\partial x_j} = -\frac{\partial p}{\partial x_i} + \frac{1}{Re}\frac{\partial^2 u_i}{\partial x_j \partial x_j}, \tag{2}$$

$$\frac{\partial c}{\partial t} + \frac{\partial c u_j}{\partial x_j} = \frac{1}{ReSc}\frac{\partial^2 c}{\partial x_j \partial x_j}, \tag{3}$$

where u_i is the instantaneous velocity in the i-th direction, p is the pressure, t is the time, and c is the scalar concentration. The notation (x_1, x_2, x_3) for the spatial coordinates is used interchangeably with the notation (x, y, z), where $z = x_3$ is the axial, i.e. streamwise, direction. Due to rotational symmetry, it is also convenient to use polar coordinates (r, θ, z), where $(x, y) = (r\cos\theta, r\sin\theta)$. All variables are non-dimensionalised with the reference quantities being the bulk velocity U_B, the pipe diameter D, and the inlet concentration c_I.

The Reynolds number is defined as $Re = \frac{U_B D}{\nu}$, where ν is the kinematic viscosity, and the Schmidt number as $Sc = \frac{\nu}{\alpha}$, where α is the scalar diffusivity. The mean (i.e. time-average) and fluctuating quantities are denoted using an overbar and a prime, for example $\overline{c}$ and c', respectively.

We perform direct numerical simulations (DNS) of a fully developed turbulent flow in a pipe of length $L = 7.5D$. The Reynolds number is $Re = 5300$, which corresponds to $Re_\tau = \frac{u_\tau R}{\nu} = 180$, where u_τ is the friction velocity and R is the radius. The flow is driven by a constant streamwise pressure gradient. For velocities, periodic boundary conditions are employed at the inlet/outlet planes, while the no-slip condition is imposed on the wall.

The passive scalar is inserted at the inlet of the pipe with uniform concentration $c(r, \theta, 0) = c_I$. We assume a totally absorbing wall with $c_W = c(R, \theta, z) = 0$. In the context of mass transfer, this boundary condition is known as a perfect sink model, which means that the scalar is irreversibly absorbed at the wall [38]. This assumption is usually applicable only at the initial stages of the deposition process, before too much deposit builds up. In the context of heat transfer, this condition corresponds to an isothermal wall. At the exit plane, a non-reflecting boundary condition is employed, $\dfrac{\partial c}{\partial t} + \dfrac{\partial u_z c}{\partial z} = 0$, where $u_z(r, \theta, L)$ is the local instantaneous axial velocity.

The governing equations are solved using an in-house unstructured finite volume solver, Pantarhei [39–42]. The convection and diffusion terms are discretised using a second-order central approximation. A third-order backward difference scheme is employed for the transient term. Orthogonal diffusion terms are treated implicitly, while the convection and non-orthogonal diffusion terms are treated explicitly using third-order extrapolation in time. The fractional step method is employed to correct velocities and pressure to satisfy the continuity equation at the end of each time step. The resulting linear systems are solved with the GMRES iterative algorithm implemented in the PETSc library [43]. Convergence is accelerated using an algebraic multigrid preconditioner from the Hypre library [44].

The grid near the centre is H-type and transitions to O-type closer to the wall to fit the cylindrical boundary, see Fig. 1(A). The cross-section is discretised with $N_{c,cross} = 3.35 \cdot 10^4$ cells and $N_z = 256$ layers are employed in the streamwise direction, resulting in a total of $N_c = 8.6 \cdot 10^6$ cells. Grid spacings (in terms of wall units) in the radial, azimuthal and axial directions are provided in table I. The ratio of the local grid size (computed as the cubic root of the cell volume) to the Kolmogorov length scale $\eta = (\nu^3/\epsilon)^{0.25}$, where ϵ is the

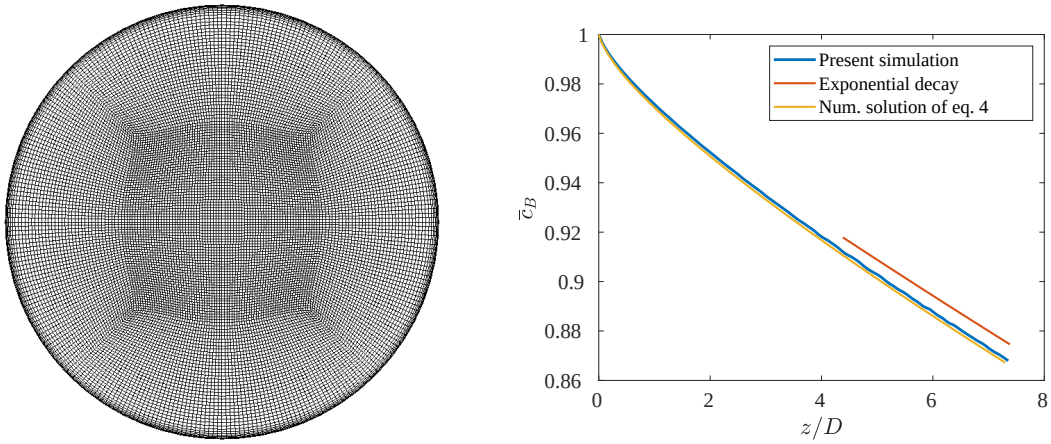

(A) (B)

FIG. 1. Cross-sectional view of the grid (A) and variation of the bulk concentration, c_B, along the axial direction, z (B).

Re_B	N_c	Δr^+_{wall}	$\Delta\theta r^+_{max}$	$\Delta r^+_{center,max}$	Δz^+	$\Delta t\left[\frac{R}{U_B}\right]$	$N_{snapshots}$
5300	$8.6\cdot10^6$	0.4	11.7	7.16	10.6	0.008	600

TABLE I. Grid parameter and time-step settings.

time-average dissipation rate, is less than 1.8 in most parts of the domain, which indicates that the flow is overall well resolved [45]. The time step is $\Delta t = 0.008\frac{R}{U_B}$, corresponding to a maximum CFL number of 0.6.

The simulation was initialized by inserting 4 counter-rotating streamwise vortices along the pipe (to trigger transition to turbulence) and continued until the flow reached statistically steady state. It was then restarted and statistics were collected over 20,000 time steps, corresponding to 160 $\frac{R}{U_B}$. In total, 600 snapshots of the 3D velocity field were stored at regular intervals (every $250\Delta t$, corresponding to $\Delta t_s = 2\frac{R}{U_B}$). The instantaneous velocity and scalar fields were interpolated into a structured cylindrical grid with $(N_r, N_\theta, N_z) = (256, 128, 256)$ data points. The database is similar in size and resolution to that of Hellstrom *et al.* [46] and 2 to 3 times larger than that of Abreu *et al.* [22].

Due to the imposed boundary conditions, a fully developed velocity and a developing scalar field are produced; snapshots of the two fields are shown in Fig. 2. Large structures with high velocities can be seen at the centre of the pipe, while the scalar fluctuations are growing in the downstream direction as a result of the imposed boundary condition. The

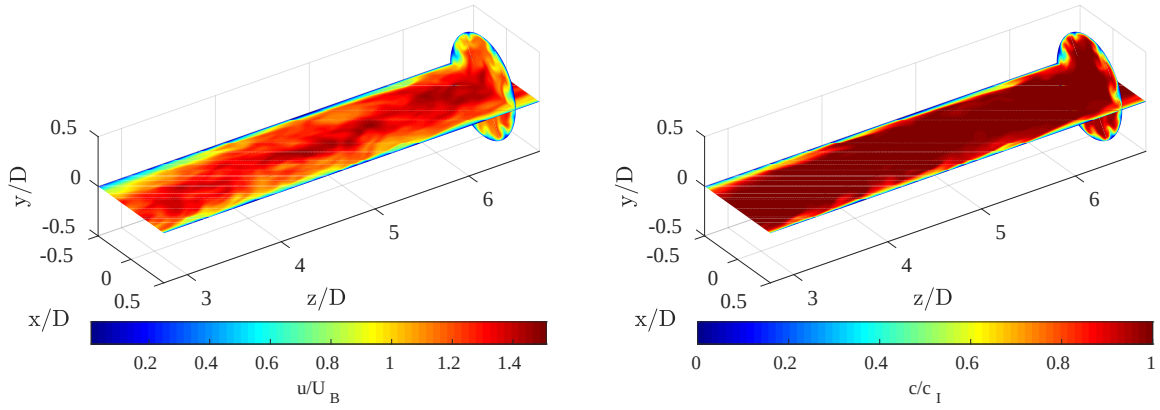

(A) (B)

FIG. 2. Contour plots of the instantaneous streamwise velocity (A) and the passive scalar (B). The flow is from left to right, and only part of the computational domain is shown in the z direction.

presence of an absorbing wall means that the section-average (or bulk) scalar concentration, defined as $\overline{c}_B = 8\int_0^{1/2} \overline{u}_z \overline{c} r \mathrm{d}r$, decreases in the streamwise direction, as shown in Fig. 1(B). By time-averaging equation (3), integrating over the cross-section of the pipe, ignoring the axial viscous term, and assuming a fully developed fluctuating scalar field, the governing equation for $\overline{c}_B$ is obtained (see also [47]),

$$\frac{\mathrm{d}\overline{c}_B}{\mathrm{d}z} + (\overline{c}_B - \overline{c}_W)\,\frac{4Sh}{ReSc} = 0, \tag{4}$$

where Sh is the Sherwood number,

$$Sh = -\frac{1}{(\overline{c}_B - \overline{c}_W)}\frac{\partial \overline{c}}{\partial r}\bigg|_{r=1/2}. \tag{5}$$

For constant Sh, equation (4) can be integrated analytically from an arbitrary location, z_0, to z and yield

$$\overline{c}_B(z) = \overline{c}_B(z_0)\exp\left[-\frac{4Sh}{ReSc}(z - z_0)\right], \tag{6}$$

where we have taken into account that $\overline{c}_W = 0$. Thus $\overline{c}_B(z)$ decays exponentially with rate $a = -\dfrac{4Sh}{ReSc} = -0.016$ (calculated for $Sh = 21.15$, see later section IV). For the range of $z - z_0$ values considered, the exponent $|a(z - z_0)| \ll 1$ and the rate of reduction is approximately linear, as shown in Fig. 1(B); the theoretical decay is superimposed in red and matches very well with the computations. Using the Sherwood number distribution

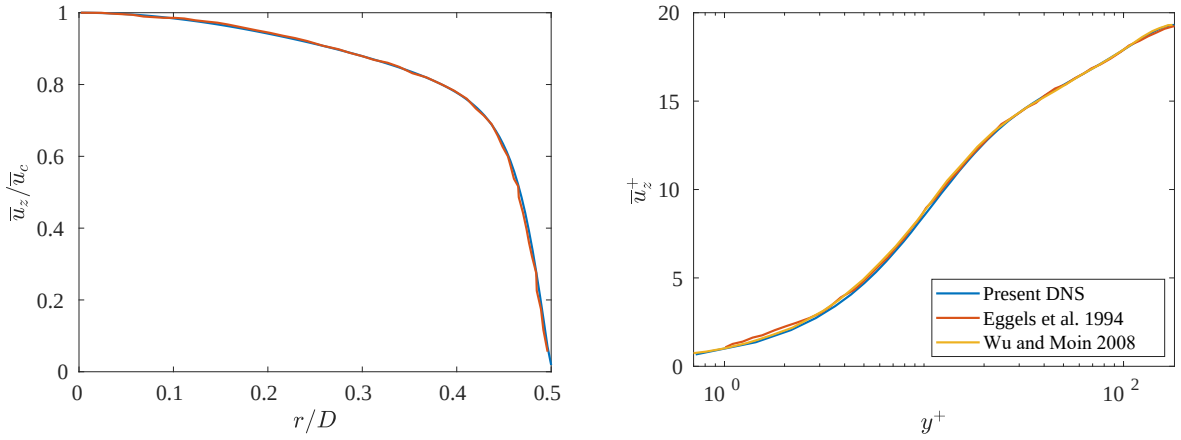

(A) (B)

FIG. 3. Variation of the mean streamwise velocity along the radial direction and comparison with results from the literature for the same Reynolds number; normalisation with global variables (A) and in wall units, denoted with a $^+$ superscript, (B).

obtained directly from the DNS (see again section IV), equation (4) can be integrated numerically. The resulting distribution of $\overline{c}_B$ is also plotted in figure 1(B). The results match well with DNS, but they are not identical, because for the derivation of (4) a fully developed fluctuating scalar field is assumed, but this is not the case close to the inlet. For the pipe length of $7.5D$ examined, $\overline{c}_B$ drops by about 14%.

The variation of the mean streamwise velocity (normalised with the value at the centre line), $\overline{u}_z/\overline{u}_c$, against r/D is shown in Fig. 3(A); the velocity plot in wall units is shown in Fig. 3(B), where $u_z^+ = \overline{u}_z/u_\tau$, $y^+ = (1-r)^+ = (1-r)u_\tau/\nu$, and u_τ is the friction velocity. The rms of the fluctuating velocities are shown in Fig. 4(A) and the Reynolds shear stress in 4(B). The averaging is taken in time and both homogeneous directions (axial and azimuthal). The present results are compared to the those of Eggels *et al.* [48] and Wu *et al.* [49] for the same Reynolds number with $3.1 \cdot 10^6$ and $6.7 \cdot 10^7$ cells respectively. Overall, both the mean and rms velocities are in good agreement with the results from the literature. The small discrepancy in the azimuthal direction is probably due to the discretisation near the wall, which is somewhat coarser compared to standard DNS.

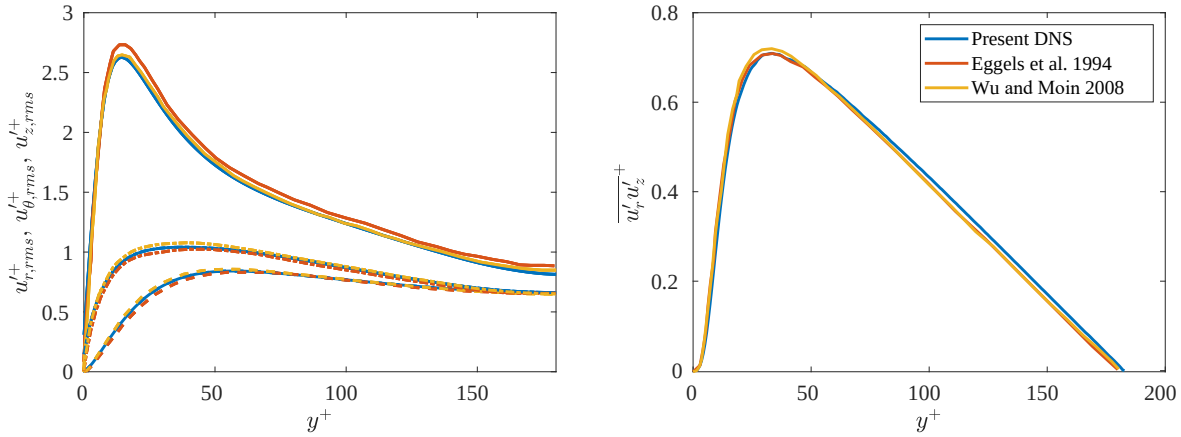

(A) (B)

FIG. 4. Variation of $u'^+_{r,rms}$, $u'^+_{\theta,rms}$, $u'^+_{z,rms}$(A) and Reynolds shear stress $\overline{u'_r u'_z}^+$ (B) along the wall-normal distance y^+ (all variables in wall units). In panel (A), the solid line represents $u'^+_{z,rms}$, the dashed line $u'^+_{r,rms}$, and the dashed-dotted line $u'^+_{\theta,rms}$.

III. PROPER ORTHOGONAL DECOMPOSITION (POD)

A. Standard POD

POD is a modal technique that decomposes a fluctuating field in terms of modes ranked according to their energy [16]. For pipe flow, we define the inner product between two fluctuating scalar or vector variables $\mathbf{q_1}$ and $\mathbf{q_2}$ as

$$\langle \boldsymbol{q}_1, \boldsymbol{q}_2 \rangle = \int_\Omega \boldsymbol{q}_1^* \boldsymbol{q}_2 r \mathrm{d}r\mathrm{d}\theta\mathrm{d}z, \tag{7}$$

where $()^*$ denotes the complex conjugate (for real variables it indicates the vector transpose). If $\mathbf{q_1} = \mathbf{q_2} = \mathbf{q}$ and $\mathbf{q}$ represents the velocity field, then $\langle \boldsymbol{q}, \boldsymbol{q} \rangle$ is equal to twice the turbulent kinetic energy integrated over the domain. It can be proven [17], that the POD modes can be found by solving an eigenvalue problem for the cross-correlation tensor $\mathbf{C} = \mathbf{q}(r, \theta, z, t)\mathbf{q}^*(r', \theta', z', t)$, which in cylindrical coordinates becomes:

$$\int_\Omega \mathbf{C}\left(r, r', \theta, \theta', z, z'\right) \phi\left(r', \theta', z'\right) r' \mathrm{d}r'\mathrm{d}\theta'\mathrm{d}z' = \lambda\phi(r, \theta, z), \tag{8}$$

where ϕ is the eigenvector and λ is the eigenvalue. The velocity or scalar fields $\mathbf{q}(r,\theta,z,t)$ can be reconstructed using these modes from,

$$\mathbf{q}(r,\theta,z,t) = \sum_{n=1}^{\infty} a_n(t)\phi_n(r,\theta,z), \tag{9}$$

where $a_n(t)$ is the temporal POD coefficient of the n-th mode. Due to homogeneity in the azimuthal direction, the cross-correlation tensor depends only on $\Delta\theta = \theta - \theta'$, which means that the POD decomposition is equivalent to Fourier expansion in the azimuthal direction [17]. Therefore, both the velocity and scalar fields are first decomposed in the azimuthal direction as

$$\mathbf{q}(r,\theta,z,t) = \sum_{m=-\infty}^{+\infty} \hat{\mathbf{q}}_m(r,z,t)\mathrm{e}^{\mathrm{i}m\theta}, \tag{10}$$

where $\hat{\mathbf{q}}_m(r,z,t)$ is the Fourier coefficient and m is the azimuthal wavenumber. The POD decomposition is then applied to the Fourier coefficients $\hat{\mathbf{q}}_m(r,z,t)$, i.e.

$$\hat{\mathbf{q}}_m(r,z,t) = \sum_{n=1}^{\infty} a_m^{(n)}(t)\phi_m^{(n)}(r,z), \tag{11}$$

where $\phi_m^{(n)}(r,z)$ is the n-th spatial mode of the m-th wavenumber. The velocity field could have been decomposed in Fourier modes in the streamwise direction as well; this is not done in the present paper however, because the scalar field is not homogeneous in this direction and thus the coupling between the velocity and scalar modes would not have been possible to observe (cf. next section).

We have implemented the method of snapshots of Sirovich [50] to evaluate the POD modes. First, a fast Fourier transform (FFT) is applied in the azimuthal direction and the Fourier-transformed snapshots are stacked column-wise in one data matrix for each wavenumber:

$$\hat{\mathbf{Q}}_m = \left[\hat{\mathbf{q}}_m^{(1)}, \hat{\mathbf{q}}_m^{(2)}, ..., \hat{\mathbf{q}}_m^{(N_t)}\right], \tag{12}$$

where $\hat{\mathbf{q}}_m^{(i)}$ indicates the i-th snapshot of the m-th wavenumber, and N_t is the total number of snapshots. We then solve the following eigenvalue problem of size N_t,

$$\frac{1}{N_t}\hat{\mathbf{Q}}_m^* \mathbf{W}\hat{\mathbf{Q}}_m\mathbf{\Psi}_m = \mathbf{\Psi}_m\mathbf{\Lambda}_m, \tag{13}$$

where $\mathbf{\Psi}_m$ is the temporal eigenvector, $\mathbf{\Lambda}_m = diag\left[\lambda_m^{(1)}, \lambda_m^{(2)}, ..., \lambda_m^{(N_t)}\right]$ is a diagonal matrix containing the eigenvalues (by convention $\lambda_m^{(1)} \geq \lambda_m^{(2)} \geq ... \geq \lambda_m^{(N_t)}$) and $\mathbf{W}$ is a weighting

matrix that accounts for the volume expansion in the radial direction. The spatial modes can be recovered from

$$\mathbf{\Phi}_m = \frac{1}{\sqrt{N_t}} \hat{\mathbf{Q}}_m \mathbf{\Psi}_m \mathbf{\Lambda}_m^{-1/2} \tag{14}$$

where $\mathbf{\Phi}_m = \left[\phi_m^{(1)}, \phi_m^{(2)}, \ldots, \phi_m^{(N_t)}\right]$. The last factor, $\mathbf{\Lambda}_m^{-1/2}$, ensures that the modes $\phi_m^{(n)}$ are orthonormal according to the inner product defined in equation (7). The matrix $\mathbf{A}_m$ of the temporal coefficients $a_m^{(n)}(t)$ that appear in equation (11) is obtained from $\mathbf{A}_m = \sqrt{N_t}\mathbf{\Lambda}_m^{1/2}\mathbf{\Psi}^*$. Keeping only the $k \ll N_t$ largest eigenvalues, we can obtain an approximate reconstruction of the flow or scalar fields for every wavenumber m from

$$\hat{\mathbf{Q}}_m^{(k)} = \sqrt{N_t}\mathbf{\Phi}_m^{(\leq k)} \mathbf{\Lambda}_m^{(\leq k)1/2} \mathbf{\Psi}_m^{(\leq k)*}, \tag{15}$$

where the superscript $(\leq k)$ denotes the truncated version of the corresponded matrices, for example $\mathbf{\Phi}_m^{(\leq k)} = \left[\phi_m^{(1)}, \phi_m^{(2)}, \ldots, \phi_m^{(k)}\right]$ and $\mathbf{\Lambda}_m^{(\leq k)} = diag\left[\lambda_m^{(1)}, \lambda_m^{(2)}, \ldots, \lambda_m^{(k)}\right]$.

B. Extended proper orthogonal decomposition

The standard POD analysis described above provides the optimal decomposition of a specific scalar or vector variable. The extended POD (EPOD), introduced by Maurell *et al.* [24] and Boree [23], can be employed to analyse correlations between different variables. The temporal basis, $\mathbf{\Psi}_m$, obtained from standard POD in one variable, is used to find the spatial modes of another, synchronised variable. It is shown in Boree [23] that the obtained EPOD modes are the only modes that are correlated with the original variable.

In this paper we aim to investigate the correlation between the velocity and scalar fluctuations. Therefore, the temporal basis obtained from the POD analysis of the scalar fluctuations will be used to decompose the velocity field. The velocity EPOD modes are obtained from:

$$\mathbf{\Phi}_{m,e} = \frac{1}{\sqrt{N_t}} \hat{\mathbf{Q}}_{m,v} \mathbf{\Psi}_{m,s} \mathbf{\Lambda}_{m,s}^{-1/2}, \tag{16}$$

where $\mathbf{\Phi}_{m,e} = \left[\phi_{m,e}^{(1)}, \phi_{m,e}^{(2)}, ..., \phi_{m,e}^{(N_t)}\right]$ is the matrix containing the EPOD modes (the subscript e stands for 'extended'), $\hat{\mathbf{Q}}_{m,v}$ is the snapshot matrix containing the Fourier-transformed velocities (as indicated by the subscript v) in the azimuthal direction, and $\mathbf{\Psi}_{m,s}$ is the temporal mode of the scalar field (indicated by the subscript, s). The kinetic energy associated with

each EPOD velocity mode is stored in the diagonal matrix

$$\mathbf{\Lambda}_{m,e} = \mathbf{\Lambda}_{m,s}\mathbf{\Phi}_{m,e}\mathbf{\Phi}^*_{m,e}\mathbf{W}, \tag{17}$$

see [23]. The energy contained in each mode will be lower compared to standard POD analysis of the velocity field, because the modes are no longer ranked based on their kinetic energy. The reconstruction of the velocity field using the k largest EPOD modes is obtained from

$$\hat{\mathbf{Q}}^{(k)}_{m,e} = \sqrt{N_t}\mathbf{\Phi}^{(\leq k)}_{m,e}\mathbf{\Lambda}^{(\leq k)1/2}_{m,s}\mathbf{\Psi}^{(\leq k)*}_{m,s}, \tag{18}$$

where we have used the same notational convention as before.

The above analysis indicates that the POD scalar modes and the velocity EPOD modes are coupled together and form a single entity. This is important for understanding some of the common features presented later in section V. The coupled modes can also be obtained by forming a combined snapshot matrix with columns that contain velocities and scalar together. The underlying inner product is a weighted generalisation of (7), with a particular form of the weighting matrix; see Appendix A for more details.

We close this section by mentioning that the recently proposed CPOD method [29] that ranks modes based on the correlation between two variables, is also applicable to our case. However for our purposes EPOD is more suitable. The latter applies standard POD to the scalar and then obtains the corresponding velocity mode which is most correlated with the scalar mode, as already mentioned. On the other hand, CPOD ranks modes based on the correlation, thus the temporal coefficient takes into account both velocity and scalar fields.

IV. FUKAGATA-IWAMOTO-KASAGI (FIK) IDENTITY FOR THE SHERWOOD NUMBER.

The FIK identity was first derived by Fukagata *et al.* [30] to quantify the laminar and turbulent contributions to the skin friction coefficient in a channel, pipe and flat plate boundary layer flow. For the present flow setting, we derive the FIK identify for the Sherwood number, defined earlier in equation (5). For the derivation, we first write the scalar transport equation (3) in polar coordinates, take the time-average, assume rotational symmetry and integrate twice over the cross section of the pipe (the details can be found in Appendix B).

The resulting expression is

$$
\begin{aligned}
Sh = & \underbrace{-\frac{8}{(\overline{c}_B - \overline{c}_W)} \int_0^1 r^2 \frac{\partial \overline{c}}{\partial r} \mathrm{d}r}_{Sh_{FIK,1}} \underbrace{+\frac{8ReSc}{(\overline{c}_B - \overline{c}_W)} \int_0^1 r^2 \overline{u_r' c'} \mathrm{d}r}_{Sh_{FIK,2}} \\
& \underbrace{+\frac{4ReSc}{(\overline{c}_B - \overline{c}_W)} \int_0^1 r(1-r^2) \left\langle \frac{\partial \overline{u}_z \overline{c}}{\partial z} \right\rangle \mathrm{d}r}_{Sh_{FIK,3}} \\
& \underbrace{+\frac{4ReSc}{(\overline{c}_B - \overline{c}_W)} \int_0^1 r(1-r^2) \left\langle \frac{\partial \overline{u_z' c'}}{\partial z} \right\rangle \mathrm{d}r}_{Sh_{FIK,4}} \\
& \underbrace{-\frac{4}{(\overline{c}_B - \overline{c}_W)} \int_0^1 r(1-r^2) \left\langle \frac{\partial^2 \overline{c}}{\partial z^2} \right\rangle \mathrm{d}r}_{Sh_{FIK,5}},
\end{aligned}
\tag{19}
$$

where $\langle\rangle$ indicates the operation

$$
\langle f \rangle = \overline{f} - 2 \int_0^1 f r \mathrm{d}r \tag{20}
$$

This formula is a special case of the FIK identity for the Nusselt number provided in [33, 35] for constant thermophysical properties. Note that in the above two equations the reference quantities for distance and velocity are the pipe radius R and twice the bulk velocity $2U_B$ (instead of D and U_B); this simplifies the resulting expression. Equation (19) indicates that the Sh number can be decomposed into a mean-field contribution, $Sh_{FIK,1}$, contributions arising from turbulent fluctuations, $Sh_{FIK,2}$, and contributions arising from axial inhomogeneity of the mean and velocity/scalar correlation fields, $Sh_{FIK,3-5}$.

The variation of Sh along the length of the pipe, obtained directly from the wall gradient (5), is shown in Fig. 5 with a solid black line. As expected, Sh attains the maximum value at the pipe inlet because the scalar boundary layer (that provides resistance to mass transfer) is thinnest at the inlet. However, Sh decays rapidly due to the growth of the scalar boundary layer, approaching asymptotically a constant value. For $z/D > 3$, Sh is practically constant (and equal to 21.15 at the exit). The asymptotic value is further compared with the empirical relationship [51],

$$
Sh = \frac{(f/8)\,(Re_B - 1000)\,Sc}{1 + 12.7(f/8)^{1/2}\,(Sc^{2/3} - 1)}, \tag{21}
$$

where $f = 0.316 Re_D^{-1/4}$ is the friction factor for a smooth pipe with $Re_B < 2 \cdot 10^4$. A value of $Sh = 19.9$ is obtained, which is marked with a horizontal dashed line in the figure. The difference compared with DNS is less than 6 %.

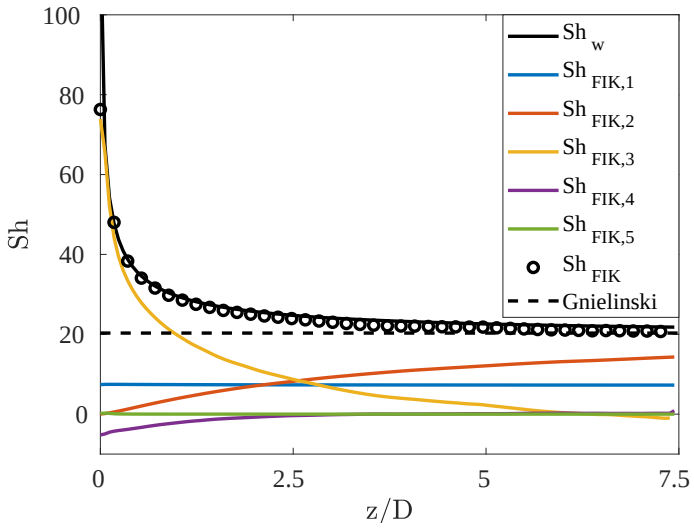

FIG. 5. Variation of Sh number and the constituent components $Sh_{FIK,1-5}$ along the length of the pipe. The horizontal black dashed line indicates the value from the empirical relation (21).

The different terms on the right hand side of equation (19) are also plotted with coloured solid lines in Fig. 5. Their sum, Sh_{FIK}, matches well with DNS; the level of accuracy is the same as in [32, 33, 35]. Close to the inlet the inhomogeneity term $Sh_{FIK,3}$ is dominant but it quickly decays, while $Sh_{FIK,2}$ grows. Terms $Sh_{FIK,4-5}$ are insignificant in the entire domain. At the exit of the pipe $Sh \approx Sh_{FIK,1} + Sh_{FIK,2}$, with $Sh_{FIK,2}$ approximately twice as large as $Sh_{FIK,1}$, and thus 65.8% of the total wall transfer is attributed to the turbulent term, $Sh_{FIK,2}$. For larger Re and/or Sc, it is expected that the contribution of $Sh_{FIK,2}$ will increase. This is indeed confirmed by the results of Nemati *et al.* [33], where the Re is the same as in our case, but $Pr = 3.19$ (the equivalent of Sc for heat transfer) and $Sh_{tot} \approx 35$, with $Sh_{FIK,2}$ approximately 80% of the Sh_{tot}.

Using the reconstructions from equations (15) and (18) we can compute the contribution of each scalar POD mode and the associated velocity EPOD mode to the correlation $\overline{u_r' c'}$ and therefore to the time average Sh. We can therefore probe the origins of $Sh_{FIK,2}$ and analyse which modes are dominant in determining the value of this term. This is the objective of the next section. To the best of the authors' knowledge, this is the first time POD/EPOD decomposition is used to quantify the effect of different modes on the time-average mass transfer to the wall using the FIK identity.

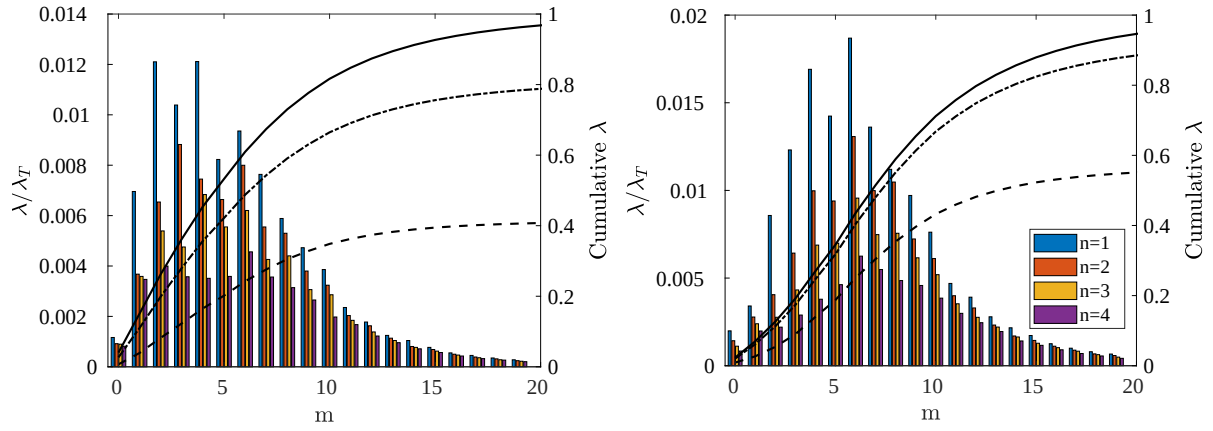

FIG. 6. Eigenvalue distribution of the velocity (A) and scalar (B) POD modes for different azimuthal wavenumbers, m. For each m, the relative energy content of $n = 1 - 4$ modes is shown with coloured vertical bars (the corresponding values are in the left axis). Lines show the cumulative energy over all wavenumbers obtained by retaining only a fixed number of POD modes for each wavenumber, m (values on the right axis). Dashed line; $n = 1 - 10$, dashed-dotted line; $n = 1 - 100$, and solid line; $n = 1 - 200$.

V. RESULTS AND DISCUSSION

A. POD modes of the velocity and scalar fields

The distribution of the eigenvalues of the standard POD modes for the velocity and scalar fields are shown in Fig. 6. For the flow field, the eigenvalues peak at azimuthal wavenumbers $m = 2 - 4, 6$, while for the scalar the eigenvalues peak at $m = 4, 6$. In general, the energy is skewed towards slightly higher wavenumbers for the scalar. Also, the relative energy of the scalar modes is larger compared to the velocity modes, meaning that fewer modes are required to reconstruct the scalar field. The same figure also shows a cumulative energy plot over all wavenumbers. Around 40% of the turbulent kinetic energy and 55% of the scalar variance can be captured by the first 10 POD modes. Larger numbers of modes (results are shown for 100 and 200) consistently capture a larger proportion of the scalar variance compared to turbulent kinetic energy, confirming that indeed fewer modes are required to describe the scalar fluctuations compared to the velocity fluctuations. The explanation for

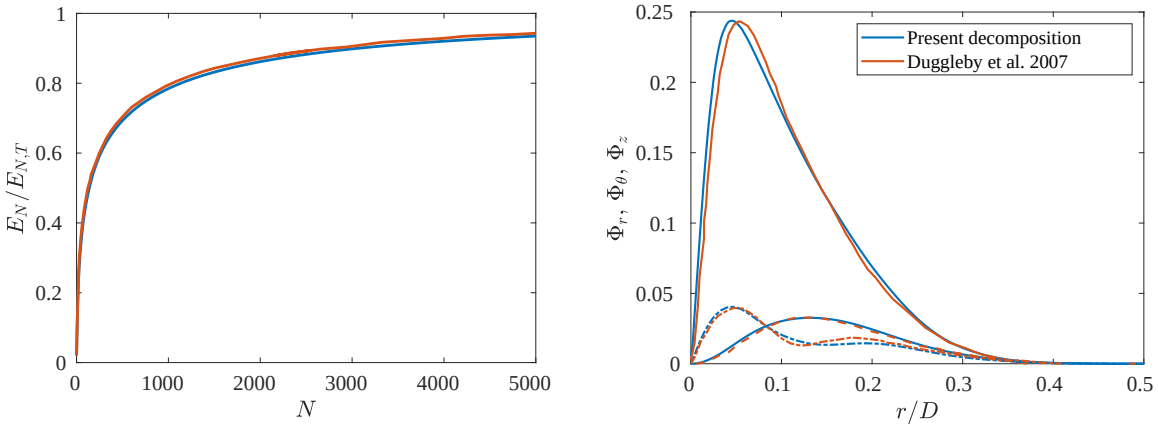

(A) (B)

FIG. 7. Cumulative energy of eigenmodes (A) and spatial distribution of the dominant mode ($n = 1$) for streamwise and azimuthal wavenumbers $k = 1$ and $m = 5$ respectively, $\phi^1_{(1,5)}$ (B). In panel (A), the blue line indicates the present results (where $Re_\tau = 180$) and the red line those of Duggleby *et al.* [18] (where $Re_\tau = 150$). In panel (B), the solid line denotes the z-component, Φ_z, of mode $\phi^1_{(1,5)}$, the dashed line the radial component, Φ_r, and the dashed-dotted line the azimuthal component, Φ_θ. The modes are normalized as in [18].

this behaviour will be provided later when the spatial distribution of the modes is analysed.

As mentioned in section III, the velocity field is decomposed in Fourier modes only in the azimuthal direction and not in the streamwise, even though both are homogeneous directions. This must be borne in mind when comparing the present results to those of Duggleby *et al.* [18], Hellstrom *et al.* [46] or Abreu *et al.* [22], where the flow is Fourier-decomposed in both directions. The main difference is a slightly different energy distribution among azimuthal wavenumbers. In Duggleby *et al.* [18] for example, where $Re_\tau = 150$, the largest eigenvalues are found at $m = 5, 6$, whereas at higher Reynolds number, [19, 46], the peaks are between $m = 2 - 4$. In the present decomposition, peaks are found at $m = 2 - 4, 6$.

In order to have a more consistent comparison with literature, the velocity field was Fourier-decomposed in both directions and subsequent POD analysis was also performed. This resulted in eigenmodes $\phi^n_{(k,m)}$, where k, m are the streamwise and azimuthal wavenumbers respectively. The results are compared to those of Duggleby *et al.* [18] in Fig. 7. Panel A shows the cumulative energy and panel B the spatial distribution of the modulus of the three components of the specific eigenmode, $\phi^1_{(1,5)}$. There are very small differences in the

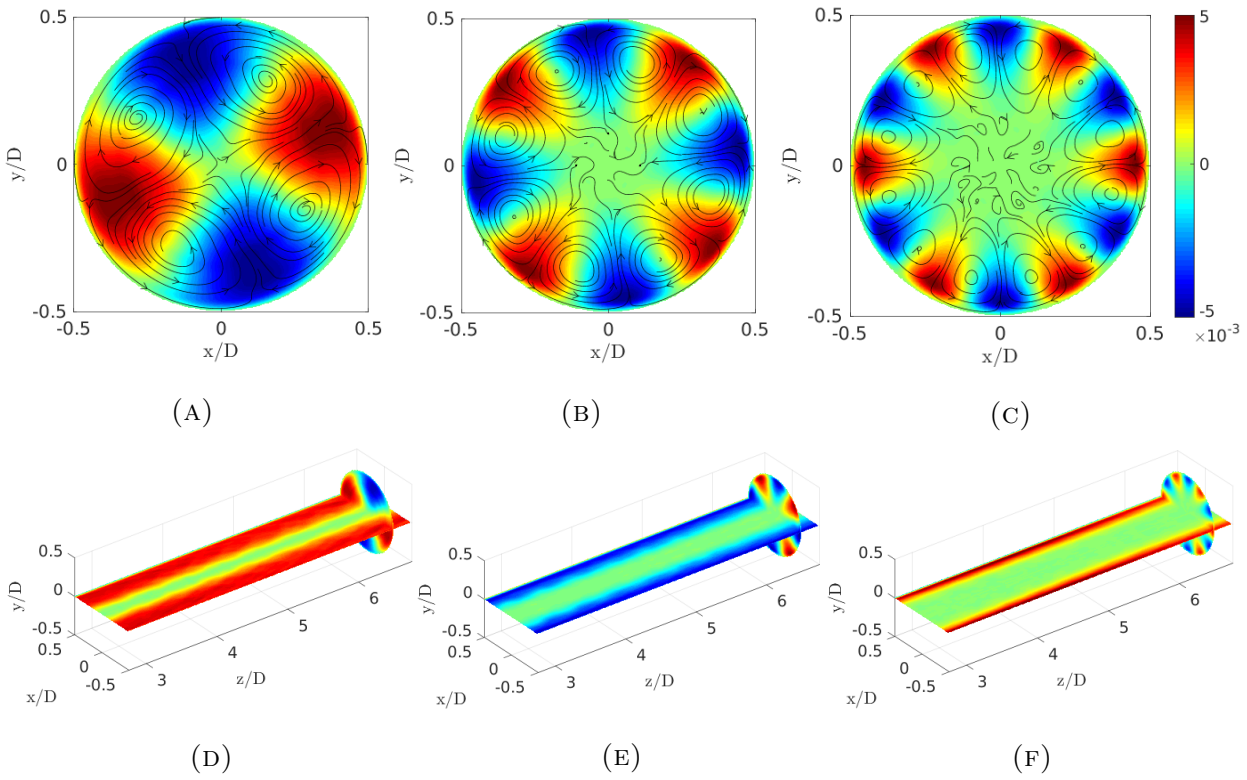

FIG. 8. Cross-section streamlines and contour plots of the z-component of the dominant velocity POD mode at $z = 6.5D$ for $m = 2$ (A), $m = 4$ (B), $m = 6$ (C), and dual-plane contour plots of t he z-component for $m = 2$ (D), $m = 4$ (E), $m = 6$ (F).

energy and shape of eigenmodes between the two sets of results, which is probably due to the slightly lower Reynolds number in Duggleby *et al.* [18]. The peak energy is found at wavenumbers $k = 1$, $m = 5 - 6$ as in [18], but the lower energy modes behave somewhat differently, most likely again due to the small difference in Reynolds number.

The shape of the streamwise velocity component of the dominant ($n = 1$) eigenmode for $m = 2, 4, 6$ is plotted in Fig. 8. The cross-stream flow is also visualised using streamlines superimposed on contours of streamwise velocity. The modes look qualitatively like the ones reported in Duggleby *et al.* [18], Baltzer *et al.* [19] and Hellstrom *et al.* [46]. For small wavenumber m the modes penetrate deeply into the core of the flow, but as m increases their presence is confined to areas closer to the wall. The closed streamline loops in the cross-stream plane transport scalar from the outer regions towards the wall (and vice versa) and contribute to the Sh, and in particular to $Sh_{FIK,2}$ component. It is exactly these contributions of velocity modes to $Sh_{FIK,2}$ that we want to quantify.

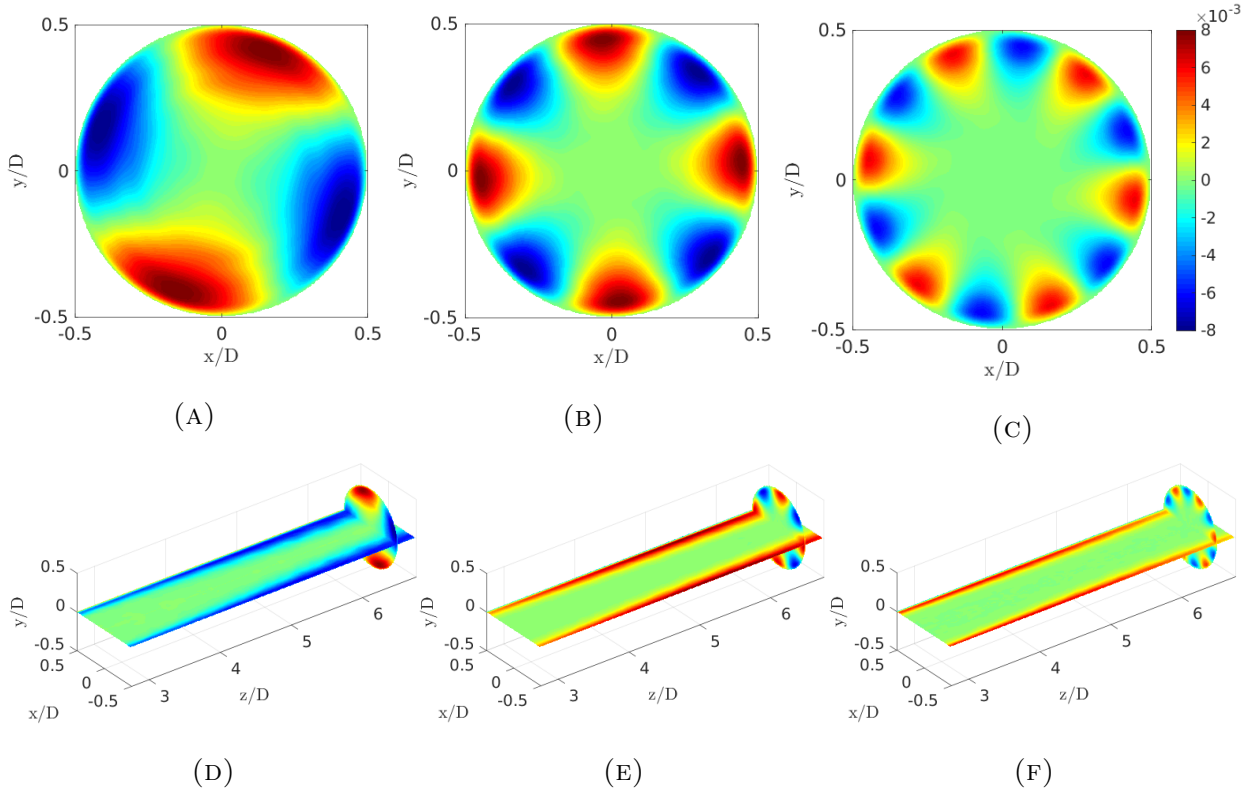

FIG. 9. Cross-section contour plots of the dominant scalar POD mode at $z = 6.5D$ for $m = 2$ (A), $m = 4$ (B), $m = 6$ (C), and dual-plane contour plots for $m = 2$ (D), $m = 4$ (E), $m = 6$ (F).

.

The dominant POD modes for the scalar (for the same m as in Fig. 8) are visualised in Fig. 9. For the higher wavenumbers, the mode shapes are similar to those of velocity. However, for $m = 2$ the penetration to the core of the flow is weaker. This is consistent with the instantaneous plots shown earlier in Fig. 2, where large velocity fluctuations can be observed around the centre line; for the scalar however the activity is confined closer to the wall, with occasional ejections towards the centre. This is expected because of the gradual growth of the scalar boundary layer, which starts at the pipe inlet and is developing within an already established underlying turbulent flow. This feature also explains why the scalar POD eigenvalues are skewed towards larger m, as shown in Fig. 6.

The previous two figures showed significant similarities, but also some differences between the velocity and scalar POD modes, especially for low m. The similarities arise from the fact that the passive scalar transport is governed by the underlying velocity field while the

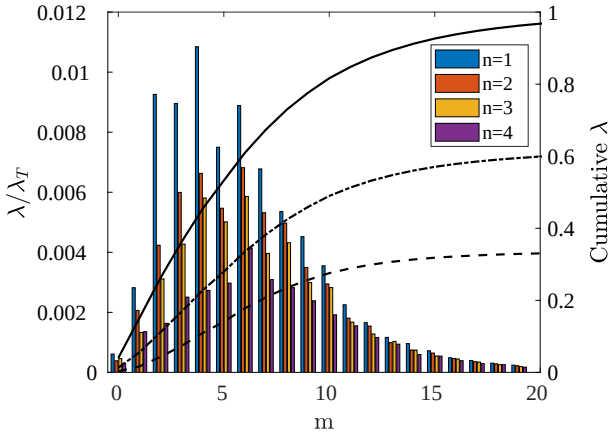

FIG. 10. Distribution of the kinetic energy of the velocity EPOD modes. The left vertical axis shows the relative energy of each mode, while the right axis shows the cumulative energy integrated over wavenumbers (dashed line for $n = 1 - 15$, dashed-dotted line for $n = 1 - 100$ and solid line for $n = 1 - 200$.)

differences are due to the developing nature of the scalar boundary layer as opposed to the fully developed turbulent flow. In order to find the velocity modes correlated with the scalar modes, we now proceed with examining the EPOD velocity modes.

B. EPOD modes of the velocity field

The kinetic energy distribution of the EPOD modes, calculated from equation (17), is plotted in Fig. 10. The shape of the distribution is similar to that of the standard POD modes shown in Fig. 6(A), however the kinetic energy of EPOD modes is lower. This indicates that the velocity modes that are most correlated with scalar fluctuations do not necessarily have much kinetic energy. This is confirmed by the cumulative distribution, also shown in Fig. 10. Indeed, the cumulative kinetic energy contained in all EPOD modes with azimuthal mode number $m = 1-20$ and $n = 1-10$ is 33%, while for $n = 1-100$ is 60% (the corresponding values for the standard velocity POD modes are 40% and 80%); for scalar modes the values are 55% and 87%, respectively. Thus velocity modes that contain, for example 60%, of the turbulent kinetic energy, are correlated with scalar modes that account for 87% of the scalar variance. This is due to the fact that scalar fluctuations are localised close to the walls of the pipe, so only the near-wall flow structures are strongly correlated

with the scalar. Velocity modes that have strong presence away from the wall become less important, since the scalar fluctuations are smaller there.

The shapes of the velocity EPOD modes are plotted in Fig. 11. A clear difference with the standard POD modes (shown in Fig. 8) can be observed in the (z, x) plane contours (bottom row in both figures). Indeed, while the dominant POD mode is constant along the streamwise direction (the contours are horizontal strips parallel to the wall), the EPOD mode shows a gradual growth, reflecting a similar behaviour for the scalar (refer to the bottom row of Fig. 9). The differences in the cross-stream (x, y) plane are more difficult to discern, but they are present. For example, the peak locations of the EPOD modes are closer to the wall compared to the POD modes; for example, for $m = 2$ at $z/D = 6.5$ the peaks are at $r/R = 0.41$ and 0.34 respectively (scalar modes peak at $r/R = 0.43$).

In Fig. 12 we collect together isosurface plots of the three modes. The similarities between the scalar (left column) and the velocity EPOD (right column) modes are very clear. There is another important feature that is also revealed in this figure; these two sets of modes are in phase in the azimuthal direction. For example, positive streamwise velocity fluctuations appear at the same θ locations as positive scalar fluctuations. This is explained by inspection of the secondary cross-stream flow patterns shown in the top row of Fig. 11. The two streamwise vortices that flank the area with positive streamwise velocity (shown in red) transport scalar from the outer flow regions to the wall. In these regions, the scalar has higher values compared to the near wall-region, thus resulting in positive fluctuations. When velocity and scalar POD modes are evaluated separately this close connection between the two fields is not apparent (refer to figures 8 and 9). It is still there, but hidden by the fact that the starting angular position in the azimuthal direction is arbitrary. Due to homogeneity in this direction, each mode can be rotated as a whole, thus when velocity and scalar modes are considered separately they have different starting angular positions. When they are considered together however, they form one entity with a single starting location, and thus the underlying connection between the two fields is clearly revealed.

At the bottom row of the Fig. 12 isosurfaces of higher-order modes are shown. They have smaller streamwise length scales, but velocity EPOD and scalar modes are still in phase.

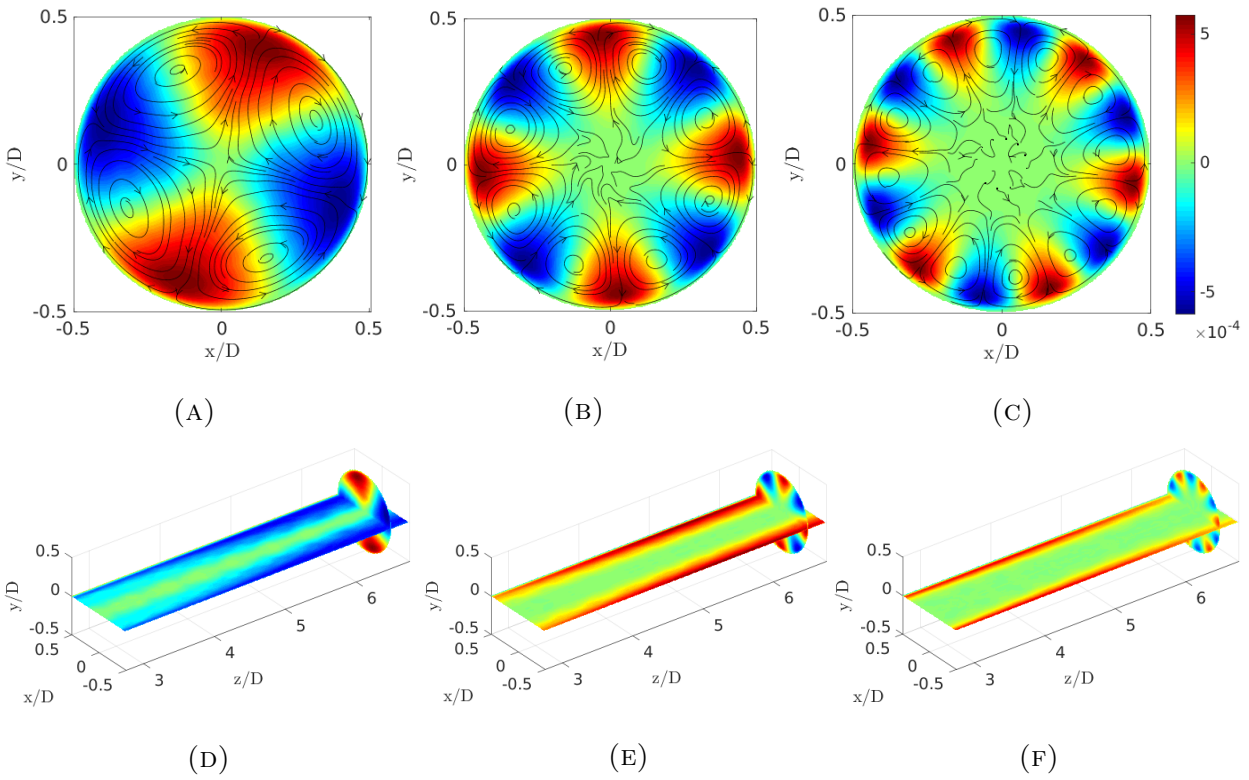

FIG. 11. Cross-section streamlines and contour plots of the z-component of the dominant velocity EPOD mode at $z = 6.5D$ for $m = 2$ (A), $m = 4$ (B), $m = 6$ (C), and dual-plane contour plot of the z-component for $m = 2$ (D), $m = 4$ (E), $m = 6$ (F).

C. Contribution of individual modes to Sh.

We can now quantify the contribution of the structures described in the previous section on the turbulent part, $Sh_{FIK,2}$, of the mass transfer coefficient, Sh, see equation (19). More specifically, the velocity EPOD and scalar POD modes for different wavenumbers m and orders n are used to reconstruct the instantaneous velocity and concentration fields and their correlation $\overline{u_r' c'}(m,n)$; the latter is then employed to compute $Sh_{FIK,2}(m,n)$.

A cumulative plot, obtained using groups of azimuthal modes, $m = 1-5$, $m = 1-10$, $m = 1-15$, $m = 1-20$ is shown in Fig. 13. This figure makes it clear that is necessary to use a large number of POD modes in order to obtain a good representation of $Sh_{FIK,2}$. A large difference in the contribution of individual wavenumbers m can observed; for example, $m = 2$ does not contribute as much compared to $m = 4-8$. This is not surprising because modes with higher m are located closer to the wall, the area with the largest fluctuations of

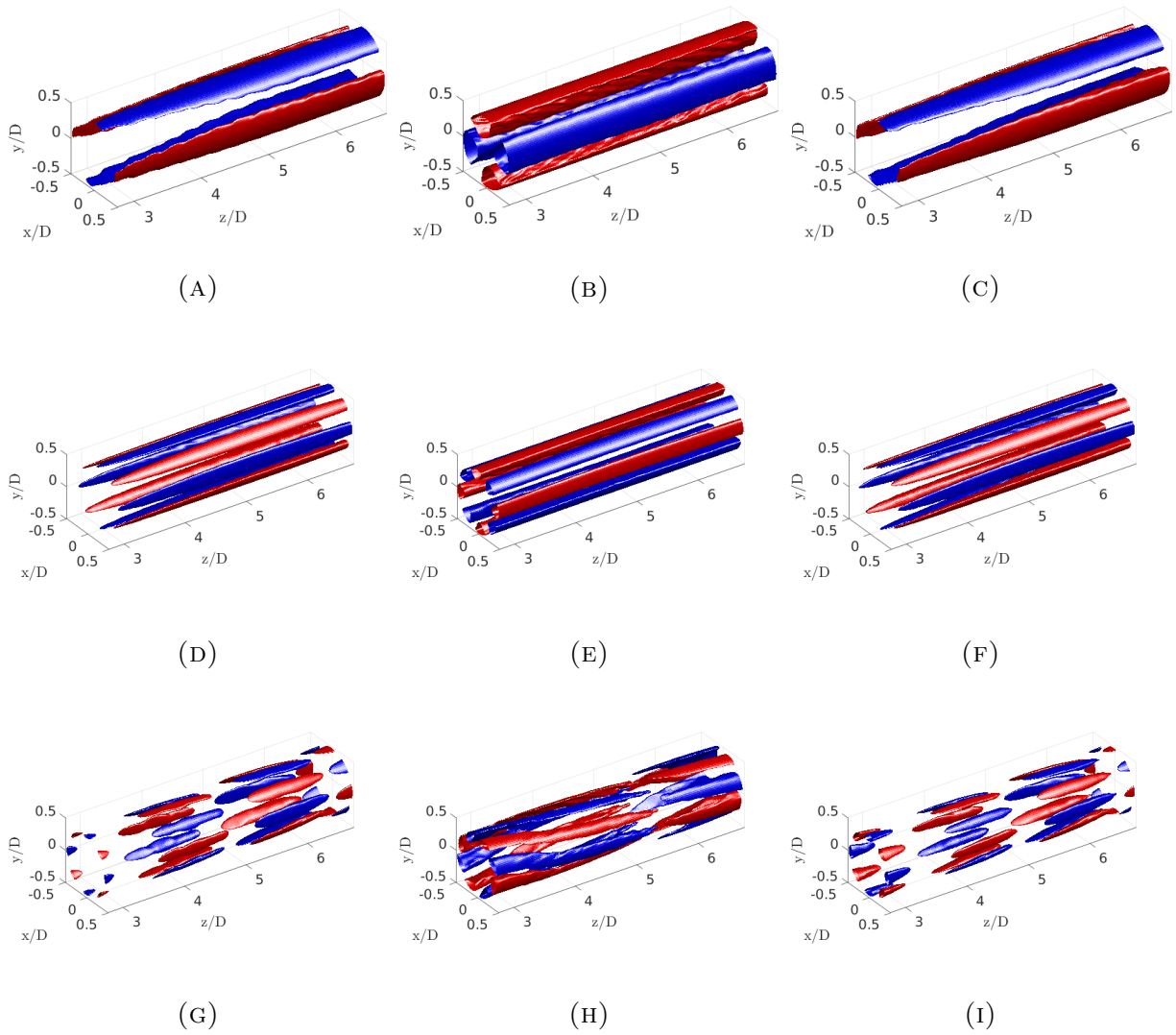

FIG. 12. Isosurfaces of scalar POD modes (left column), POD streamwise velocity modes (middle column) and EPOD streamwise velocity modes (right column). Top row; $m = 2$, $n = 1$, middle row; $m = 4$, $n = 1$ and bottom row; $m = 4$, $n = 4$. The isosurfaces correspond to 50% of maximum positive (red) and negative (blue) value.

c. The cumulative plot in Fig. 13 indicates that a substantial proportion of $Sh_{FIK,2}$, equal to about 38%, can be reconstructed using the wavenumber group $m = 1 - 10$ and mode orders $n = 1 - 10$.

Instantaneous maps of the Sherwood number and of the streamwise fluctuating velocity at the cylindrical surface located at $y^+ = 15$ are shown in figures 14 and 15 respectively. The figures display both the DNS results (left panel) and the reconstructed fields (right panel). For the selected range of m and n (refer to figure caption), 49% of the turbulent

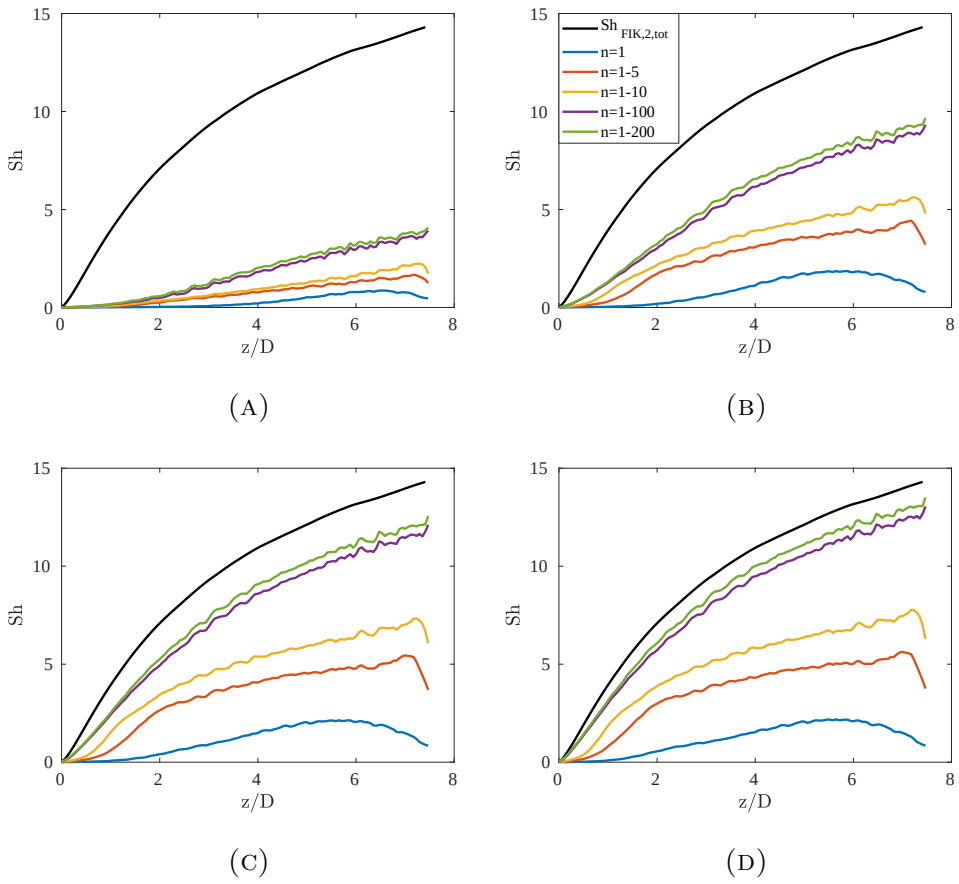

FIG. 13. Cumulative $Sh_{FIK,2}(m_1 : m_2, n_1 : n_2) = \sum_{m=m_1}^{m_2} \sum_{n=n_1}^{n_2} Sh_{FIK,2}(m,n)$ using wavenumber groups $m = 1-5$ (A), $m = 1-10$ (B) $m = 1-15$ (C) and $m = 1-20$ (D). Results with different mode orders n are indicated with lines of different colour.

part of the time-average wall transfer can be reconstructed. It is clear that truncation of the EPOD velocity modes acts as a low-pass filter, removing small-scale structures from the flow. Notice also the dominant role of the coherent structures in the wall transfer process. Indeed, there is a very clear correlation between the maps of the flow structures and the Sh number, exactly as established and described in the previous section. These two figures also explain the need for at least a moderate number of mode order, n. Orders $n > 1$ are associated with streamwise ligaments, as shown in the bottom row of Fig. 12, that are necessary to capture the instantaneous inhomogeneity in the z direction.

We now consider the integral of $Sh_{FIK,2}$ over the length of the pipe, $\Gamma_T = \int_0^L Sh_{FIK,2} \mathrm{d}z$,

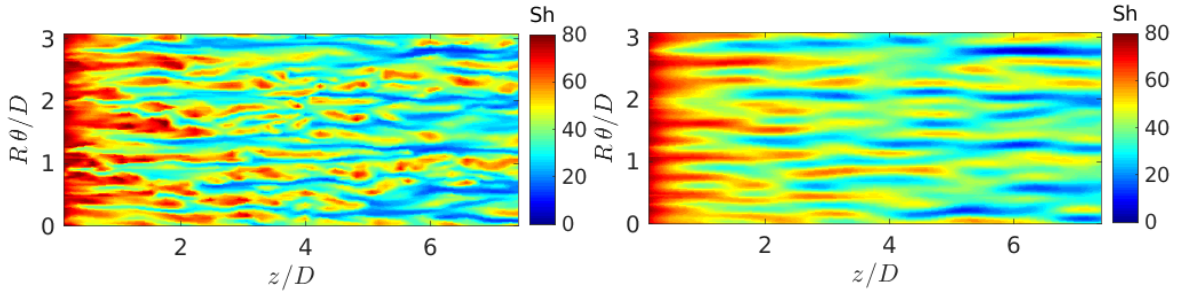

(A) (B)

FIG. 14. Contour plot of the instantaneous Sherwood number, DNS result (A), reconstructed map using $m = 1 - 15$ and $n = 1 - 10$ (B). The vertical axis denotes the normalised perimeter (from 0 to π).

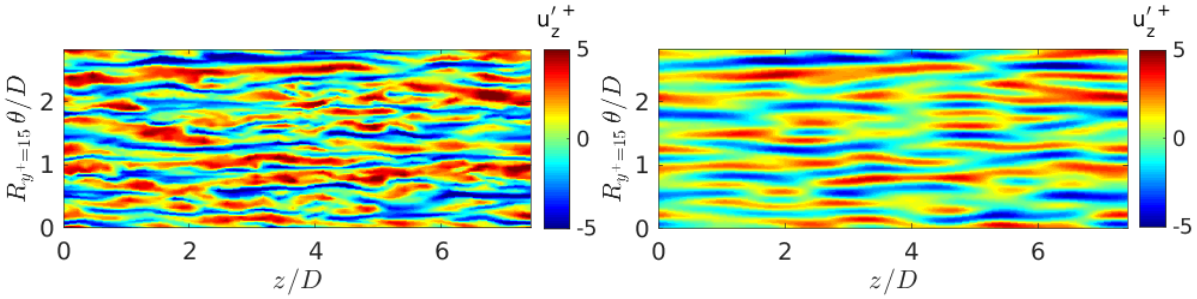

(A) (B)

FIG. 15. Contour plot of the instantaneous streamwise fluctuating velocity, $u_z'^+$, at $y^+ = 15$ (A), and reconstructed velocity field using EPOD modes $m = 1 - 15$ and $n = 1 - 10$ (B). The vertical axis denotes the normalised perimeter (from 0 to π).

which we decompose as $\Gamma_T = \sum_m \sum_n \Gamma(m,n)$ where

$$\Gamma(m,n) = \int_0^L Sh_{FIK,2}(m,n)\mathrm{d}z. \tag{22}$$

The ratio Γ/Γ_T is plotted in Fig. 16 for different values of m and n. It can be seen that $\Gamma(m,n)$ has large values in the region $m = 4-8$ (the maximum is at $m = 6$), which indicates that it is the near-wall turbulent structures that contribute most strongly to the wall mass transfer. This can be also seen from the gradient of the curves that represent the cumulative Γ, also shown in Fig. 17, which is maximised in the aforementioned region of m. Fig. 17(A) shows the cumulative Γ for a wider range of n, shown using symbols, for single values and groups of wavenumbers, m, where the horizontal axis is the kinetic energy or scalar variance

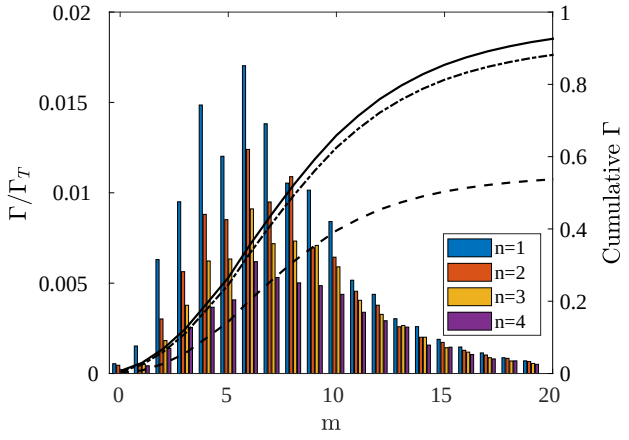

FIG. 16. Ratio Γ/Γ_T for different wavenumbers, m, and POD numbers, n (left axis). The right axis shows the cumulative ratio summed over wavenumbers $m = 0 - 20$ (dashed line is $n = 1 - 15$, dashed-dotted line is $n = 1 - 100$, and the solid line is $n = 1 - 200$)

and the vertical axis is the ratio Γ/Γ_T. For example, the single wavenumber $m = 6$ (dashed yellow line), which corresponds to the peak in Fig. 16, is responsible for about 9% of the total wall mass transfer, while the group $m = 1 - 5$ (solid blue line) accounts for 20%. If we focus on the range $m = 1-15$ and $n = 1-10$, then approximately 49% can be reconstructed. This group of $m \times n = 150$ modes (omitting modes with negative m) correspond to only about 0.4% of the total number of available POD modes.

To provide further insight, we now analyse the contribution of each mode in relation to its kinetic energy; which is also plotted in Fig. 17(A) for single wavenumbers and 17(B) for groups of wavenumbers. Intuitively, the larger the energy of a mode, the more it will contribute to the total wall transfer, so we expect a positive correlation. The steeper the slope, the larger the contribution of a mode for a given turbulent kinetic energy or scalar variance. As can be seen from Fig. 17(A), there is a large spread in the slopes of the velocity EPOD modes (solid lines), but the spread is much smaller for the slope of scalar modes (dashed lines). Interestingly, while velocity EPOD modes with $m = 6$ may have the largest overall contribution to the wall transfer in absolute terms (solid yellow line in Fig. 17(A), modes with $m = 8$ have a slightly larger slope, and are thus more efficient. Fig. 17(B) shows that increasing the range of m values, the cumulative transfer reaches an asymptotic relation with respect to the kinetic energy contained within the EPOD modes. This slope is larger compared to the one relating the transfer and the variance of scalar modes.

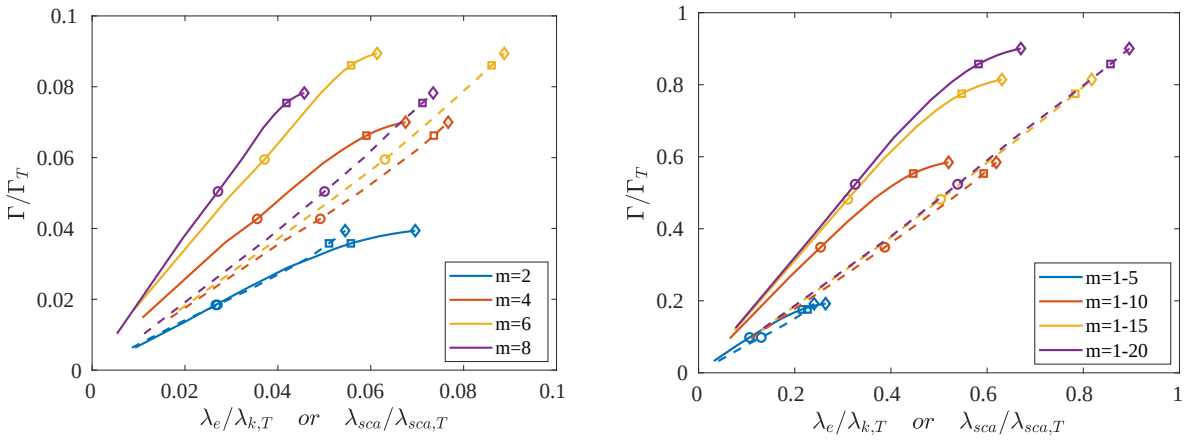

(A) (B)

FIG. 17. Γ/Γ_T plotted against eigenvalues for single wavenumbers (A) and groups of wavenumbers (B). In both figures, solid lines represent eigenvalues from velocity EPOD modes, and dashed lines eigenvalues from scalar POD modes. A circle corresponds to $n = 1 - 10$, a square to $n = 1 - 100$ and a diamond to $n = 1 - 200$.

D. Quadrant analysis

We further investigate the fractional contributions of the instantaneous velocity and scalar fluctuations to the turbulent scalar flux $\overline{u_r'c'}$ that appears in $Sh_{FIK,2}$ using quadrant analysis. The signs of the velocity and scalar fluctuations partition the (c', u_r') plane in 4 quadrants. In quadrant Q_1 we have $u_r' > 0$ and $c' > 0$, in Q_2 $u_r' > 0$ and $c' < 0$, in Q_3 $u_r' < 0$ and $c' < 0$, and finally in Q_4 $u_r' < 0$ and $c' > 0$. The first quadrant, Q_1, is associated with sweep events (fluid elements with high scalar concentration move towards the wall), while Q_3 is associated with ejection events (elements with low scalar concentration are ejected away from the wall). The second quadrant, Q_2, represents motion of fluid particles with high concentration away from the wall, and finally Q_4 contains motion towards the wall of low concentration particles (more details can be found in the review of Wallace [52]).

The turbulent flux in the radial direction, $\overline{u_r'c'}$, can be written as

$$\overline{u_r'c'} = \int_{-\infty}^{+\infty} \int_{-\infty}^{+\infty} u_r'c' P(u_r', c') \mathrm{d}u_r' \mathrm{d}c', \tag{23}$$

where $P(u_r', c')$ is the joint probability density function (JPDF) and $u_r'c'P(u_r', c')$ is the weighted JPDF. In order to elucidate the contribution of each quadrant to the scalar flux,

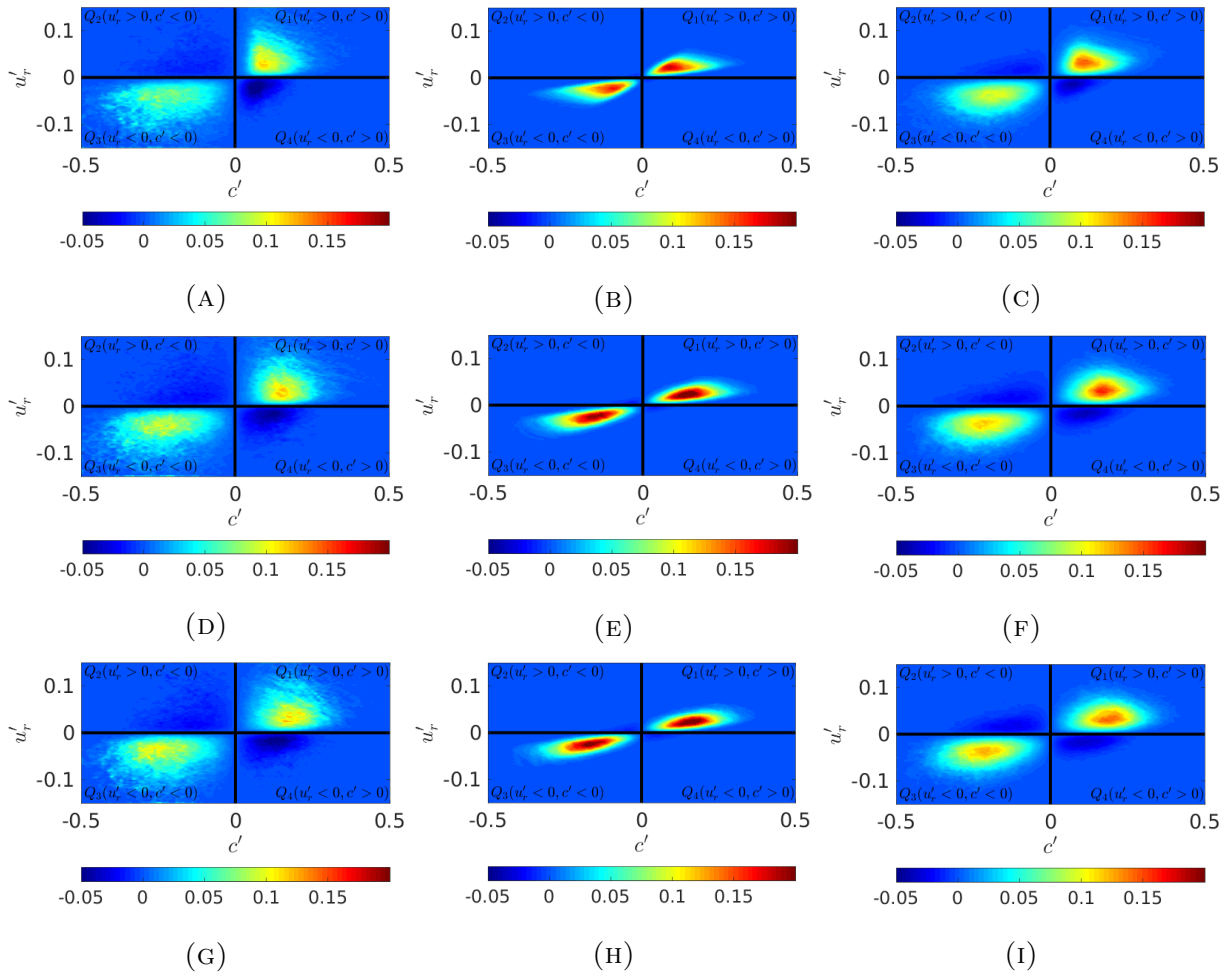

FIG. 18. Contour plots of the weighted probability density function at $y^+ = 15 - 30$. Top row (panels A,B,C) is for $z/D = 2$, middle row (panels D,E,F) is for $z/D = 4$ and bottom row (panels G, H, I) is for $z/D = 6.5$. Left column (panels A,D,G) is from DNS data, middle column (panels B,E,H) is from low order reconstruction with $m = 1 - 15$ and $n = 1 - 10$, and right column (panels C,F,I) is from a high order reconstruction with $m = 1 - 20$ and $n = 1 - 100$.

contours of the weighted JPDF evaluated at three streamwise locations are shown in Fig. 18. The DNS results, depicted in the left column of the figure, indicate that the most significant contribution to $\overline{u_r' c'}$ arises from Q_1 and Q_3; this clearly indicates the importance of the sweep and ejection events. We further investigate the ability of the reconstructed velocity and scalar fields using EPOD and POD modes respectively to capture the DNS behavior. In Fig. 18 results are presented for mode groups $m = 1 - 15$ and $n = 1 - 10$ (middle column) as well as $m = 1 - 20$ and $n = 1 - 100$ (right column). The former (low

order) reconstruction results in an almost symmetric pattern of sweep and ejection events and no Q_2 and Q_4 events are produced. Such a reconstruction clearly cannot reproduce the richness of the DNS results. Note also that it has larger peaks than the DNS. The reason is that the range of values for u_r' and c' is more narrow; see for example smaller u_r' value range compared with the DNS and the higher order reconstruction. A more narrow range leads to the overshoot of the JPDF values (to preserve an integral of 1) and this to an overshoot of the weighted JPDF. On the other hand, the higher-order reconstruction is much closer to DNS but still clips some of the largest (and more rare) magnitudes of the scalar and velocity fluctuations. Furthermore, events in Q_2 and Q_4 have now made an appearance.

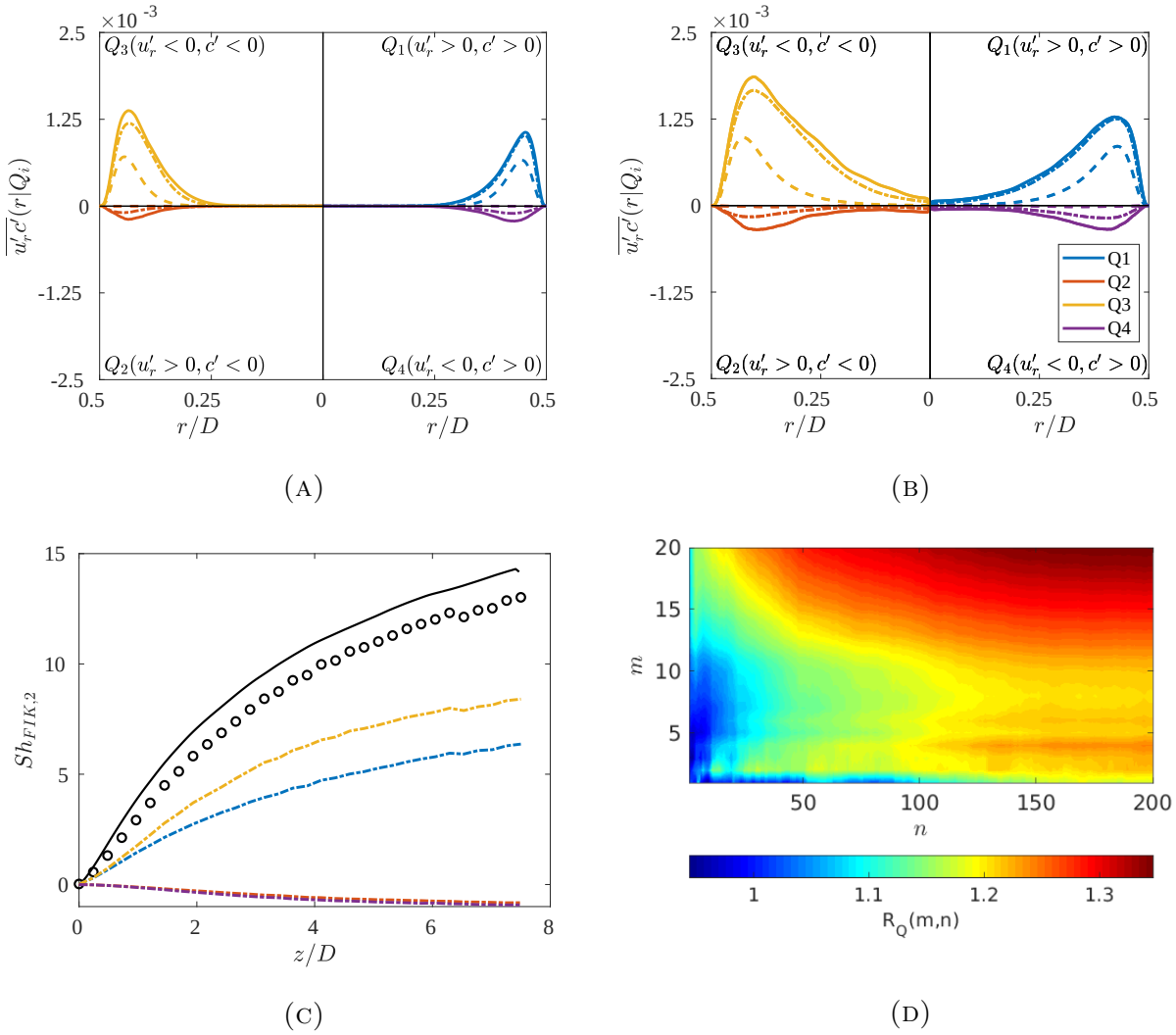

FIG. 19. In panels (A-B), the conditional fluxes $\overline{u_r'c'}(r|Q_i)$ are plotted at $z/D = 2$ and $z/D = 6.5$ and in panel (C) these fluxes are used to evaluate the components $Sh_{FIK,2}|Q_i$, see equation (25). The dashed line denotes $m = 1 - 15$ and $n = 1 - 10$, the dashed-dotted line $m = 1 - 20$ and $n = 1 - 100$ and the solid line denotes values directly from DNS data. In panel (C), the circles denote $Sh_{FIK,2} = \sum_{i=1}^{4} Sh_{FIK,2}|Q_i$, the solid black line denotes DNS values and the other colours and line types are the same as in panels (A,B) (only data for $m = 1 - 20$ and $n = 1 - 100$ are shown). Panel (D) shows contours of the ratio $R_Q(m,n) = \frac{Sh_{FIK,2}|Q_3}{Sh_{FIK,2}|Q_1}$ at $z/D = 6.5$.

The effect of the mode parameters on the quality of reconstruction is further analysed in Fig. 19. The weighted JPDFs at several radial locations were computed and integrated over each quadrant; the results are shown for 2 streamwise locations, $z/D = 2$ and 6.5, in

panels A and B respectively (top row). For example, the quantity plotted against r in the top-right square of panel A (denoted as Q_1) is

$$\overline{u_r'c'}(r|Q_1) = \int_0^{+\infty}\int_0^{+\infty} u_r'c'P(u_r',c')\mathrm{d}u_r'\mathrm{d}c'. \tag{24}$$

The PDF was computed using the DNS data as well as reconstructed field data for the two (m,n) combinations considered in Fig. 18. These plots confirm that the low order reconstruction only contributes to Q_1 and Q_3, whereas the high order one contributes to all quadrants. The more accurate reconstruction also indicates that Q_3 makes the largest contribution, i.e. ejection (rather than sweep) events play the dominant role, which is also observed in Nagano and Tagawa (1988) [53]. The conditioned turbulent fluxes peak close to the wall and grow in the streamwise direction, in agreement with figures 11 and 5 respectively. Furthermore, both the high order reconstruction and the DNS data show that Q_2 and Q_4 events have almost equal contribution.

The conditional turbulent fluxes, $\overline{u_r'c'}(r|Q_i)$, can be used to decompose $Sh_{FIK,2}$ as

$$Sh_{FIK,2} = \sum_{i=1}^{4} Sh_{FIK,2}|Q_i = \sum_{i=1}^{4} \frac{8ReSc}{(\overline{c}_B - \overline{c}_W)} \int_0^1 \overline{u_r'c'}(r|Q_i)r^2\mathrm{d}r \tag{25}$$

The variation of the components $Sh_{FIK,2}|Q_i$ in the streamwise direction is shown in Fig. 19C. Close to the entrance, where the scalar field is rapidly developing, the contributions of Q_1 and Q_3 are very similar. Further downstream, however, the contribution of Q_3 starts to dominate. This is further investigated in Fig. 19D, where contours of the ratio

$$R_Q(m,n) = \frac{Sh_{FIK,2}|Q_3}{Sh_{FIK,2}|Q_1} = \frac{\int_0^1 \overline{u_r'c'}(r|Q_3)(m,n)r^2\mathrm{d}r}{\int_0^1 \overline{u_r'c'}(r|Q_1)(m,n)r^2\mathrm{d}r}, \tag{26}$$

are plotted in the (m,n) plane. The figure shows that the asymmetry increases for growing wavenumber, m, and POD number, n.

VI. CONCLUSIONS

In this paper, we investigated the role of coherent structures on passive scalar transport and wall transfer in a turbulent pipe flow at $Re = 5300$ (based on bulk velocity). The methodology presented has allowed us to analyse individual coherent structures and link them to the time-average wall transfer coefficient.

The scalar structures were identified with POD, while the flow structures were correlated with those of the scalar with EPOD. Both velocity and scalar fields were Fourier-transformed in the homogeneous azimuthal direction and expressed in terms of azimuthal wavenumbers, m. The POD analysis reveals that wavenumbers $m = 4-6$ have the highest scalar variance, with the velocity modes peaking in slightly smaller m. Visualisation of modes allows us to gain insight into the scalar transport mechanism. Velocity POD and EPOD modes are qualitatively similar, but EPOD modes have weaker presence in the core of the pipe. Recirculating patterns in the cross-section transport scalar from the outer flow regions towards the wall and vice-versa.

Using the FIK identity, we evaluated the contribution of turbulent scalar flux to the time-average Sherwood number, Sh. We found that up to 65.8% of Sh is due to velocity/scalar correlations; the exact value depends on the axial location. POD and EPOD modes were subsequently employed to decompose the correlations and analyse the contribution of individual modes to Sh. The results indicate that the dominant mode with azimuthal wavenumber $m = 6$ has the largest contribution to Sh. In general, near-wall structures with wavenumbers $m = 4-8$ contribute mostly to Sh, especially when considering their relatively low turbulent kinetic energy. By combining modes with $m = 1 - 15$ and $n = 1 - 10$, it is possible to reconstruct 49% of the turbulent component of the wall transfer coefficient; these modes contain only 31% of the kinetic energy. Finally, using quadrant analysis we quantified the contribution of sweep and ejection events and found that ejection events, located in the third quadrant, dominate.

Future work will explore the potential of the methodology for gaining insight into more complex settings that may include inertial particles, chemical reactions and different flow configurations. This approach can also be exploited to actively or passively control the wall transfer rate, in the same way that the understanding of the effect of different flow structures in the skin friction have recently led to the developments of drag reducing actuation strategies that offer net power savings, even in large Re numbers [37].

ACKNOWLEDGEMENT

The authors would like to thank the UK Turbulence Consortium, `www.ukturbulence.co.uk`, for providing computational time at the UK supercomputing facility ARCHER via

EPSRC Grant No. EP/R029326/1. We are also grateful to the UK Materials and Molecular Modelling Hub, partially funded by EPSRC (EP/P020194/1), for computational resources on THOMAS. The authors would also like to acknowledge the financial support from the Leverhulme Trust (RPG-2018-101).

APPENDIX A: COMPARISON BETWEEN POD AND EPOD

In EPOD the inner product between two fluctuating vector variables $\mathbf{q_1}$ and $\mathbf{q_2}$ takes the form

$$\langle \boldsymbol{q}_1, \boldsymbol{q}_2 \rangle_E = \int_\Omega \boldsymbol{q}_1^* \boldsymbol{W}' \boldsymbol{q}_2 \; r \mathrm{d}r \mathrm{d}\theta \mathrm{d}z, \tag{27}$$

where $\boldsymbol{W}'$ is a weighting matrix. If $\boldsymbol{W}' = \boldsymbol{I}$ i.e the identity matrix, this definition is the same as for standard POD, equation (7). For EPOD however, some of the variables are given zero weight. For example, in our case vectors $\mathbf{q_1}$ and $\mathbf{q_2}$ contain both velocity and scalar fields (for instance $\boldsymbol{q_1} = [u_{r_1}, u_{\theta_1}, u_{z_1}, c_1]^{\mathrm{T}}\,(r, \theta, z)$) and the weighting matrix $\boldsymbol{W}'$ is diagonal with the elements corresponding to the velocity field set equal to $\mathbf{0}$, i.e. $\boldsymbol{W}' = \mathrm{diag}\,(\mathbf{0}, \mathbf{0}, \mathbf{0}, \mathbf{1})$.

Assuming the finite volume method is used, the discrete form of equation (27) is

$$\langle \boldsymbol{q}_1, \boldsymbol{q}_2 \rangle_E = \boldsymbol{q}_1^* \boldsymbol{W} \boldsymbol{q}_2, \tag{28}$$

where $\boldsymbol{W}$ is the product of $\boldsymbol{W}'$ and a diagonal matrix $\boldsymbol{V}$ containing the grid cell volumes, i.e. $\boldsymbol{W} = \mathrm{diag}\,(\mathbf{0}, \mathbf{0}, \mathbf{0}, \boldsymbol{V})$. Performing snapshot POD on the 4 variables simultaneously, one obtains a temporal eigenvector satisfying,

$$\frac{1}{N_t} \boldsymbol{Q}_{comb}^* \boldsymbol{W} \boldsymbol{Q}_{comb} \boldsymbol{\Psi} = \boldsymbol{\Psi} \boldsymbol{\Lambda}, \tag{29}$$

where $\boldsymbol{Q}_{comb}$ is the combined snapshot matrix with columns that contain both velocity and scalar. However, due to the structure of the weighting matrix $\boldsymbol{W}$, the solution is the same as the one arising from applying standard POD to the scalar only. The spatial modes, obtained from

$$\boldsymbol{\Phi} = \frac{1}{\sqrt{N_t}} \mathbf{Q}_{comb} \boldsymbol{\Psi} \boldsymbol{\Lambda}^{-1/2} \tag{30}$$

contain both the POD scalar modes and the EPOD velocity modes.

APPENDIX B: DERIVATION OF THE FIK IDENTITY.

The FIK identity for a passive scalar is derived in this appendix; the process is similar to that of Kasagi *et al.* [31] and Nemati *et al.* [33]. The dimensionless scalar transport equation written in polar coordinates is

$$\frac{\partial c}{\partial t}+u_r\frac{\partial c}{\partial r}+\frac{u_\theta}{r}\frac{\partial c}{\partial \theta}+u_z\frac{\partial c}{\partial z}=\frac{1}{ReSc}\left[\frac{1}{r}\frac{\partial}{\partial r}\left(r\frac{\partial c}{\partial r}\right)+\frac{1}{r^2}\frac{\partial^2 c}{\partial \theta^2}+\frac{\partial^2 c}{\partial z^2}\right], \tag{31}$$

where distances are normalised with the radius R, velocities with twice the bulk velocity $2U_B$, and scalar concentration with the value at the inlet, c_I. The Reynolds-averaged form of (31) is

$$0=\frac{1}{r}\frac{\partial}{\partial r}r\left[\overline{u_r'c'}-\frac{1}{ReSc}\frac{\partial \overline{c}}{\partial r}\right]-\frac{1}{ReSc}\frac{\partial^2\overline{c}}{\partial z^2}+\frac{\partial \overline{u}_z\overline{c}}{\partial z}+\frac{\partial\overline{u_z'c'}}{\partial z}, \tag{32}$$

where we have assumed that the time-average flow is axisymmetric, i.e. $\overline{u}_\theta=0$, $\frac{\partial\overline{c}}{\partial\theta}=0$, and has only an axial component, i.e. $\overline{u}_r=0$. Setting

$$\overline{I}_z=-\frac{1}{ReSc}\frac{\partial^2\overline{c}}{\partial z^2}+\frac{\partial \overline{u}_z\overline{c}}{\partial z}+\frac{\partial\overline{u_z'c'}}{\partial z} \tag{33}$$

as the streamwise in homogeneity term, we get the simpler form

$$0=\frac{1}{r}\frac{\partial}{\partial r}r\left[\overline{u_r'c'}-\frac{1}{ReSc}\frac{\partial \overline{c}}{\partial r}\right]+\overline{I}_z, \tag{34}$$

The Sherwood number at the wall is defined as:

$$Sh=-\frac{2kR}{\alpha}=-2\left.\frac{d\overline{c}}{dr}\right|_{wall}\frac{1}{\overline{c}_B-\overline{c}_W} \tag{35}$$

where $k=\dfrac{J_w}{\overline{c}_B-\overline{c}_W}$ is the mass transfer coefficient, $J_w=\alpha\left.\dfrac{\partial\overline{c}}{\partial r}\right|_{wall}$ is the wall flux and α is the diffusivity.

Equation (32) is integrated over the cross-section of the pipe,

$$0=\int_0^1\frac{1}{r}\frac{\partial}{\partial r}r\left[\overline{u_r'c'}-\frac{1}{ReSc}\frac{\partial\overline{c}}{\partial r}\right]r\mathrm{d}r+\int_0^1\overline{I}_z r\mathrm{d}r\Rightarrow 0=-\left.\frac{1}{ReSc}\frac{\partial\overline{c}}{\partial r}\right|_{wall}+\int_0^1\overline{I}_z r\mathrm{d}r \tag{36}$$

Equation (36) is now multiplied with 2 and subtracted from (32),

$$0=\frac{1}{r}\frac{\partial}{\partial r}r\left[\overline{u_r'c'}-\frac{1}{ReSc}\frac{\partial\overline{c}}{\partial r}\right]+\langle I_z\rangle+\left.\frac{2}{ReSc}\frac{\partial\overline{c}}{\partial r}\right|_{wall}, \tag{37}$$

where for a generic variable f we have defined the operator $\langle f\rangle=\overline{f}-2\int_0^1 fr\mathrm{d}r$. Integrating (37) over a cross-section of radius r we get,

$$\begin{aligned}0&=\int_0^r\frac{1}{r}\frac{\partial}{\partial r}r\left[\overline{u_r'c'}-\frac{1}{ReSc}\frac{\partial\overline{c}}{\partial r}\right]r\mathrm{d}r+\int_0^r\langle I_z\rangle r\mathrm{d}r+\int_0^r\left.\frac{2}{ReSc}\frac{\partial\overline{c}}{\partial r}\right|_{wall}r\mathrm{d}r\Rightarrow\\ \frac{Sh(\overline{c}_B-\overline{c}_W)}{ReSc}\frac{r^2}{2}&=r\left[\overline{u_r'c'}-\frac{1}{ReSc}\frac{\partial\overline{c}}{\partial r}\right]+\int_0^r\langle I_z\rangle r\mathrm{d}r\end{aligned} \tag{38}$$

where the definition of Sherwood number, equation (35), was used. Finally, (38) is integrated again over the cross-section of the pipe,

$$\begin{aligned}\int_0^1 \frac{Sh(\overline{c}_B-\overline{c}_W)}{ReSc}\frac{r^2}{2}r\mathrm{d}r &= \int_0^1 r\left[\overline{u_r'c'}-\frac{1}{ReSc}\frac{\partial\overline{c}}{\partial r}\right]r\mathrm{d}r+\int_0^1\int_0^r\langle I_z\rangle r\mathrm{d}r r\mathrm{d}r \Rightarrow \\ \frac{Sh(\overline{c}_B-\overline{c}_W)}{ReSc}\frac{1}{8} &= \int_0^1 r\overline{u_r'c'}r\mathrm{d}r-\frac{1}{ReSc}\int_0^1 r\frac{\partial\overline{c}}{\partial r}r\mathrm{d}r+\int_0^1\int_0^r\langle I_z\rangle r\mathrm{d}r r\mathrm{d}r\end{aligned} \tag{39}$$

Using integration by parts, the final expression for the FIK identity becomes

$$\begin{aligned}Sh = &-\frac{8}{(\overline{c}_B-\overline{c}_W)}\int_0^1 r\frac{\partial\overline{c}}{\partial r}r\mathrm{d}r+\frac{8ReSc}{(\overline{c}_B-\overline{c}_W)}\int_0^1 r\overline{u_r'c'}r\mathrm{d}r+ \\ &\frac{4ReSc}{(\overline{c}_B-\overline{c}_W)}\int_0^1(1-r^2)\left(\left\langle\frac{\partial\overline{u}_z\overline{c}}{\partial z}\right\rangle+\left\langle\frac{\partial\overline{u_z'c'}}{\partial z}\right\rangle\right)r\mathrm{d}r-\frac{4}{(\overline{c}_B-\overline{c}_W)}\int_0^1(1-r^2)\left\langle\frac{\partial^2\overline{c}}{\partial z^2}\right\rangle r\mathrm{d}r.\end{aligned} \tag{40}$$

This form is used in the rest of the paper.

---

[1] N. Hutchins and I. Marusic, "Evidence of very long meandering features in the logarithmic region of turbulent boundary layers," *Journal of Fluid Mechanics*, vol. 579, pp. 1–28, 2007.

[2] A. J. Smits, B. J. McKeon, and I. Marusic, "High–Reynolds Number Wall Turbulence," *Annual Review of Fluid Mechanics*, vol. 43, no. 1, pp. 353–375, 2011.

[3] J. Jiménez, "Coherent structures in wall-bounded turbulence," *Journal of Fluid Mechanics*, vol. 842, p. P1, 2018.

[4] B. J. McKeon, "The engine behind (wall) turbulence: Perspectives on scale interactions," *Journal of Fluid Mechanics*, vol. 817, pp. 1–86, 2017.

[5] J. Kim and P. Moin, "Transport of passive scalars in a turbulent channel flow," *Turbulent Shear Flows 6*, pp. 85–96, 1989.

[6] H. Abe, H. Kawamura, and Y. Matsuo, "Surface heat-flux fluctuations in a turbulent channel flow up to Re_τ=1020 with Pr=0.025 and 0.71," *International Journal of Heat and Fluid Flow*, vol. 25, no. 3, pp. 404–419, 2004.

[7] H. Kawamura, K. Ohsaka, H. Abe, and K. Yamamoto, "DNS of turbulent heat transfer in channel flow with low to medium-high prandtl number fluid," *International Journal of Heat and Fluid Flow*, vol. 19, no. 5, pp. 482–491, 1998.

[8] H. Kawamura, H. Abe, and Y. Matsuo, "Dns of turbulent heat transfer in channel flow with

respect to Reynolds and Prandtl number effects," *International Journal of Heat and Fluid Flow*, vol. 20, no. 3, pp. 196–207, 1999.

[9] H. Kawamura, H. Abe, and Y. Matsuo, "Very large-scale structures observed in DNS of turbulent channel flow with passive scalar transport," in *Australasian Fluid Mechanics Conference*, 2004.

[10] S. Pirozzoli, M. Bernardini, and P. Orlandi, "Passive scalars in turbulent channel flow at high Reynolds number," *Journal of Fluid Mechanics*, vol. 788, pp. 614–639, 2016.

[11] R. Gurka, A. Liberzon, and G. Hetsroni, "Detecting coherent patterns in a flume by using PIV and IR imaging techniques," *Experiments in Fluids*, vol. 37, no. 2, pp. 230–236, 2004.

[12] H. Nakamura, N. Shiibara, and S. Yamada, "Quantitative measurement of spatio-temporal heat transfer to a turbulent water pipe flow," *International Journal of Heat and Fluid Flow*, vol. 63, pp. 46–55, 2017.

[13] S. T. Dawson, B. J. McKeon, and T. Saxton-Fox, "Modeling passive scalar dynamics in wall-bounded turbulence using resolvent analysis," *2018 AIAA Fluid Dynamics Conference*, p. 4042, 2018.

[14] A. Laskari, T. Saxton-Fox, and B. J. McKeon, "Spatial organisation of velocity structures for large passive scalar gradients," *Journal of Fluid Mechanics*, vol. 885, p. A33, 2020.

[15] F. Mallor, M. Raiola, C. Sanmiguel Vila, R. Örlü, S. Discetti, and A. Ianiro, "Modal decomposition of flow fields and convective heat transfer maps: An application to wall-proximity square ribs," *Experimental Thermal and Fluid Science*, vol. 102, pp. 517–527, 2019.

[16] J. L. Lumley, "Atmospheric Turbulence and Radio Wave Propagation," in *Proceedings of the international Colloquium Moscow*, pp. 166–176, 1965.

[17] P. Holmes, J. L. Lumley, G. Berkooz, and C. W. Rowley, *Turbulence, Coherent Structures, Dynamical Systems and Symmetry*. Cambridge: Cambridge University Press, 2nd ed., 2012.

[18] A. Duggleby, K. S. Ball, M. R. Paul, and P. F. Fischer, "Dynamical eigenfunction decomposition of turbulent pipe flow," *Journal of Turbulence*, vol. 8, no. 43, pp. 1–24, 2007.

[19] J. R. Baltzer, R. J. Adrian, and X. Wu, "Structural organization of large and very large scales in turbulent pipe flow simulation," *Journal of Fluid Mechanics*, vol. 720, pp. 236–279, 2013.

[20] L. H. Hellström, B. Ganapathisubramani, and A. J. Smits, "The evolution of large-scale motions in turbulent pipe flow," *Journal of Fluid Mechanics*, vol. 779, no. August, pp. 701–715, 2015.

[21] J. H. Lee, H. J. Sung, and R. J. Adrian, "Space-time formation of very-large-scale motions in turbulent pipe flow," *Journal of Fluid Mechanics*, vol. 881, pp. 1010–1047, 2019.

[22] L. I. Abreu, A. V. Cavalieri, P. Schlatter, R. Vinuesa, and D. S. Henningson, "Spectral proper orthogonal decomposition and resolvent analysis of near-wall coherent structures in turbulent pipe flows," *Journal of Fluid Mechanics*, vol. 900, p. A11, 2020.

[23] J. Borée, "Extended proper orthogonal decomposition: A tool to analyse correlated events in turbulent flows," *Experiments in Fluids*, vol. 35, no. 2, pp. 188–192, 2003.

[24] S. Maurel, J. Borée, and J. L. Lumley, "Extended proper orthogonal decomposition: Application to jet/vortex interaction," *Flow, Turbulence and Combustion*, vol. 67, no. 2, pp. 125–136, 2001.

[25] C. Hoarau, J. Borée, J. Laumonier, and Y. Gervais, "Analysis of the wall pressure trace downstream of a separated region using extended proper orthogonal decomposition," *Physics of Fluids*, vol. 18, no. 5, 2006.

[26] A. Antoranz, A. Ianiro, O. Flores, and M. García-Villalba, "Extended proper orthogonal decomposition of non-homogeneous thermal fields in a turbulent pipe flow," *International Journal of Heat and Mass Transfer*, vol. 118, pp. 1264–1275, 2018.

[27] P. A. Kadu, Y. Sakai, Y. Ito, K. Iwano, M. Sugino, T. Katagiri, T. Hayase, and K. Nagata, "Application of spectral proper orthogonal decomposition to velocity and passive scalar fields in a swirling coaxial jet," *Physics of Fluids*, vol. 32, no. 1, p. 15106, 2020.

[28] C. Duwig and P. Iudiciani, "Extended proper orthogonal decomposition for analysis of unsteady flames," *Flow, Turbulence and Combustion*, vol. 84, no. 1, pp. 25–47, 2010.

[29] A. V. G. Cavalieri and A. F. C. da Silva, "Cross proper orthogonal decomposition," *Phys. Rev. Fluids*, vol. 6, p. 014602, Jan 2021.

[30] K. Fukagata, K. Iwamoto, and N. Kasagi, "Contribution of Reynolds stress distribution to the skin friction in wall-bounded flows," *Physics of Fluids*, vol. 14, no. 11, pp. L73–L76, 2002.

[31] N. Kasagi, Y. Hasegawa, K. Fukagata, and K. Iwamoto, "Control of turbulent transport: Less friction and more heat transfer," *Journal of Heat Transfer*, vol. 134, no. 3, 2012.

[32] J. Lee, S. Y. Jung, H. J. Sung, and T. A. Zaki, "Turbulent thermal boundary layers with temperature-dependent viscosity," *International Journal of Heat and Fluid Flow*, vol. 49, no. C, pp. 43–52, 2014.

[33] H. Nemati, A. Patel, B. J. Boersma, and R. Pecnik, "The effect of thermal boundary condi-

tions on forced convection heat transfer to fluids at supercritical pressure," *Journal of Fluid Mechanics*, vol. 800, pp. 531–556, 2016.

[34] P. Zhao, J. Zhu, Z. Ge, J. Liu, and Y. Li, "Direct numerical simulation of turbulent mixed convection of LBE in heated upward pipe flows," *International Journal of Heat and Mass Transfer*, vol. 126, pp. 1275–1288, 2018.

[35] S. Pandey, X. Chu, E. Laurien, and B. Weigand, "Buoyancy induced turbulence modulation in pipe flow at supercritical pressure under cooling conditions," *Physics of Fluids*, vol. 30, no. 6, p. 65105, 2018.

[36] S. Straub, P. Forooghi, L. Marocco, T. Wetzel, R. Vinuesa, P. Schlatter, and B. Frohnapfel, "The influence of thermal boundary conditions on turbulent forced convection pipe flow at two Prandtl numbers," *International Journal of Heat and Mass Transfer*, vol. 144, p. 118601, 2019.

[37] I. Marusic, D. Chandran, A. Rouhi, M. K. Fu, D. Wine, B. Holloway, D. Chung, and A. J. Smits, "An energy-efficient pathway to turbulent drag reduction," *Nature Communications*, vol. 12, p. 5805, 2021.

[38] M. Elimelech, J. Gregory, X. Jia, and R. Williams, *Particle deposition and aggregation, measurement, modeling and simulation*, vol. 125. Butterworth-Heinemann, 1 ed., 1995.

[39] K. Mikhaylov, S. Rigopoulos, and G. Papadakis, "Reconstruction of large-scale flow structures in a stirred tank from limited sensor data," *AIChE Journal*, p. e17348, 2021.

[40] H. Yao, F. Alves-Portela, and G. Papadakis, "Evolution of conditionally averaged second-order structure functions in a transitional boundary layer," *Phys. Rev. Fluids*, vol. 5, p. 093902, Sep 2020.

[41] I. Paul, G. Papadakis, and J. C. Vassilicos, "Genesis and evolution of velocity gradients in near-field spatially developing turbulence," *Journal of Fluid Mechanics*, vol. 815, pp. 295–332, 2017.

[42] H. Y. Tang, S. Rigopoulos, and G. Papadakis, "A methodology for coupling DNS and discretised population balance for modelling turbulent precipitation," *International Journal of Heat and Fluid Flow*, vol. 86, no. March, 2020.

[43] S. Balay, S. Abhyankar, M. Adams, J. Brown, P. Brune, K. Buschelman, L. Dalcin, A. Dener, V. Eijkhout, W. Gropp, D. Karpeyev, D. Kaushik, M. Knepley, D. May, L. Curfman McInnes, R. Mills, T. Munson, K. Rupp, K. Sanan, B. Smith, S. Zampini, and H. Zhang, "PETSc Users

Manual Revision 3.13," tech. rep., 2016.

[44] R. D. Falgout and U. M. Yang, "Hypre: A library of high performance preconditioners," in *Computational Science — ICCS 2002* (P. M. A. Sloot, A. G. Hoekstra, C. J. K. Tan, and J. J. Dongarra, eds.), (Berlin, Heidelberg), pp. 632–641, Springer Berlin Heidelberg, 2002.

[45] S. B. Pope, *Turbulent Flows*. Cambridge University Press, 2000.

[46] L. H. Hellström and A. J. Smits, "Structure identification in pipe flow using proper orthogonal decomposition," *Philosophical Transactions of the Royal Society A: Mathematical, Physical and Engineering Sciences*, vol. 375, no. 2089, 2017.

[47] F. P. Incropera, D. P. DeWitt, T. L. Bergman, and A. S. Lavine, *Fundamentals of Heat and Mass Transfer*. New York: John Wiley & Sons, Inc., 6th edition ed., 2007.

[48] J. G. M. Eggels, F. Unger, M. H. Weiss, J. Westerweel, R. J. Adrian, R. Friedrich, and F. T. Nieuwstadt, "Fully developed turbulent pipe flow: A comparison between direct numerical simulation and experiment," *Journal of Fluid Mechanics*, vol. 268, no. June, pp. 175–210, 1994.

[49] X. Wu and P. Moin, "A direct numerical simulation study on the mean velocity characteristics in turbulent pipe flow," *Journal of Fluid Mechanics*, vol. 608, pp. 81–112, 2008.

[50] L. Sirovich, "Turbulence and the dynamics of coherent structures part I: coherent structures," *Quarterly of Applied Mathematics*, vol. 45, no. 3, pp. 561–571, 1987.

[51] V. Gnielinski, "New equations for heat and mass transfer in turbulent pipe and channel flow," *International Chemical Engineering*, vol. 16, no. 2, pp. 359–368, 1976.

[52] J. M. Wallace, "Quadrant Analysis in Turbulence Research: History and Evolution," *Annual Review of Fluid Mechanics*, vol. 48, pp. 131–158, 2016.

[53] Y. Nagano and M. Tagawa, "Statistical characteristics of wall turbulence with a passive scalar," *Journal of Fluid Mechanics*, vol. 196, p. 157–185, 1988.